

TOPICAL REVIEW

Recent progress in near-field nanolithography using light interactions with colloidal particles: from nanospheres to three-dimensional nanostructures

To cite this article: Xu A Zhang *et al* 2019 *Nanotechnology* **30** 352002

View the [article online](#) for updates and enhancements.



IOP | ebooksTM

Bringing you innovative digital publishing with leading voices to create your essential collection of books in STEM research.

Start exploring the collection - download the first chapter of every title for free.

Topical Review

Recent progress in near-field nanolithography using light interactions with colloidal particles: from nanospheres to three-dimensional nanostructures

Xu A Zhang¹, I-Te Chen² and Chih-Hao Chang² ¹Chemical and Biomolecular Engineering, University of Pennsylvania, Philadelphia, PA 19104, United States of America²Department of Mechanical and Aerospace Engineering, North Carolina State University, Raleigh, NC 27695, United States of AmericaE-mail: chichang@ncsu.edu

Received 4 March 2019

Accepted for publication 17 May 2019

Published 11 June 2019



CrossMark

Abstract

The advance of nanotechnology is firmly rooted in the development of cost-effective, versatile, and easily accessible nanofabrication techniques. The ability to pattern complex two-dimensional and three-dimensional nanostructured materials are particularly desirable, since they can have novel physical properties that are not found in bulk materials. This review article will report recent progress in utilizing self-assembly of colloidal particles for nanolithography. In these techniques, the near-field interactions of light and colloids are the sole mechanisms employed to generate the intensity distributions for patterning. Based on both ‘bottom-up’ self-assembly and ‘top-down’ lithography approaches, these processes are highly versatile and can take advantage of a number of optical effects, allowing the complex 3D nanostructures to be patterned using single exposures. There are several key advantages including low equipment cost, facile structure design, and patterning scalability, which will be discussed in detail. We will outline the underlying optical effects, review the geometries that can be fabricated, discuss key limitations, and highlight potential applications in nanophotonics, optoelectronic devices, and nanoarchitected materials.

Keywords: colloidal particles, self-assembly, nanosphere, 3D nanolithography, 3D nanostructures

(Some figures may appear in colour only in the online journal)

1. Introduction

Nanostructures and their fabrication techniques have remained highly active research areas in both industry and academia due to their unique properties that are not found at the macroscopic scale. Combining both material composition and structure geometry, nanostructured materials have novel applications in nanophotonics [1–31], mechanical metamaterials [32–37],

biomimetic surfaces [38–42], energy storage [43, 44], and biomedical devices [45–49]. Among the various structural types, three-dimensional (3D) nanostructures are especially interesting and have enabled a number of key innovations in nanoscience and nanotechnology in recent years. However, fabricating 3D structures over large area remains challenging, and most work has been limited to small-scale laboratory demonstrations. Improving feature resolution, patterning precision, geometry

complexity, and system throughput have been the central challenges in nanomanufacturing [50]. The ability to fabricate nanostructure in a scalable, cost-effective manner would greatly accelerate nanotechnology research, enable macroscale implementation, and facilitate the transition to commercialization.

Existing ‘top-down’ lithography approaches share a common hardware approach to patterning, which relies heavily on expensive optical, electrical, and mechanical components [51–86]. These include electron-beam lithography [51–53], focused ion beam lithography [54–56], probe-based methods [57–61], and two-photon polymerization [62–65]. Another advantage of these techniques is arbitrary geometry patterning, which is critical for small-scale device demonstration. They also can have high resolution, but are generally serial processes with low throughput. Similar to writing with a pen, scaling over large area becomes increasingly problematic as feature size reduces, thereby increasing patterning time significantly. While there are efforts to adopt multiple-probe architectures, existing prototypes have yet to show the same precision as single-probe systems [57]. Recent advances in nanoimprint lithography using thermal and UV-curable processes [66–70] have also dramatically improved the ability to pattern high resolution features with nanoscale precision [71]. However, these techniques rely on the replication of a high-quality master pattern, which still require the use of probed-based techniques mentioned above. These techniques are also mostly planar in nature, and layer-by-layer processing is required to patterned 3D geometry where overlay accuracy and multiple patterning can increase process cost.

Laser interference lithography [72–79] is an effective method for patterning of periodic 3D nanostructures due to its parallel nature. However, these systems require sophisticated hardware, extensive system realignment when changing lattice parameter. While these efforts are well suited in laboratory setting, they are difficult to scale for manufacturing. Another 3D patterning method is phase mask lithography using a transparent prism or mask [80–86]. These techniques rely on the interference of light to create periodic nanostructures. However, the patterns generated in these systems are tied to system configuration or prism and mask geometry, which need to be altered when new pattern geometries are required. Therefore, like the previous techniques, it relies on complicated hardware to generate the original pattern. This can be cumbersome and expensive for prototyping, since changing the desired 3D structure would require new masks. Therefore, the versatility of these approaches is limited.

In addition to ‘top-down’ lithography, spontaneous self-assembly of elementary components into organized geometries is a promising ‘bottom-up’ nanofabrication method [87–122]. The assembly geometry reflects the most energy-favorable configuration using inter-element forces in the absence of complex system hardware. Such assembly systems have led to high-density nanostructures, and examples include block copolymers [87–92], DNA [93–95], and colloidal particles [96–109]. Monodispersed colloids with spherical geometry, also known as micro/nanospheres, are particularly interesting, and can form 2D hexagonal close-packed

structures when dispersed on a planar surface. Colloidal spheres can also assemble into 3D geometry known as the opal structure [97–99]. However, defects and yield over whole substrates are still problematic in comparison with 2D monolayer assembly. While these elegant systems can organize nanoscale structures at low cost, current methods provide limited geometry control for 3D architectures. For example, assembly of nanospheres can only yield hexagonal close-packed structures in 2D and opal/inverse-opal structures in 3D. Therefore, while self-assembly systems have low cost, the lack of geometry control has presented limitations in terms of pattern versatility.

It can be seen that both ‘top-down’ and ‘bottom-up’ approaches have their own distinct advantages and limitations. This review will focus on a hybrid approach that examines the interaction of light and self-assembled colloidal elements for near-field nanolithography. This class of techniques is based on simple optical phenomena, such as light focusing, scattering, diffraction, and other near-field effects, and are inexpensive compared to conventional lithography techniques. The simple elegance of these nanolithography techniques allow for scalability and high throughput in the production of complex 2D and 3D nanostructures. This approach takes advantage of the pattern resolution, precision, and versatility of the lithography approach, while retaining the low cost and scalability seen in self-assembly system. In this review, a brief history of using colloidal nanospheres for lithography will be reviewed. The focusing and scattering of light from a single sphere and their applications for nanolithography will then be discussed. The diffraction and interference of light from an array of nanospheres will also be examined, which can lead to scalable 3D nanolithography. The scalability and challenges are analyzed for these two techniques. Applications of these near-field patterning techniques will be highlighted, and a conclusion and outlook will be given at the end of this review.

2. Colloidal assembly and its interactions with light

The self-assembly of monodispersed micro/nanospheres on a planar surface has been a promising technique to generate a periodic structure array, and was first used as a tool for nanopatterning using the term ‘natural lithography’ [110]. In this work 500 nm polystyrene (PS) nanospheres were assembled into a hexagonal array on a silicon wafer using spincoating. Later the term nanosphere lithography (NSL) was adopted [111, 112], and the assembled nanospheres were used as a lift-off mask for metal evaporation. This process then creates the inverse pattern, generating an array of triangles. The nanosphere array can be used as a physical mask for subtractive processes, such as plasma and reactive ion etching processes often used in standard micromachining. Using these methods, nanostructures in a variety of substrates and devices have been demonstrated [113–120]. While these techniques are effective in creating surface structures, these additive and subtractive processes do not increase the pattern complexity. In other words, the geometries obtained are either the same or

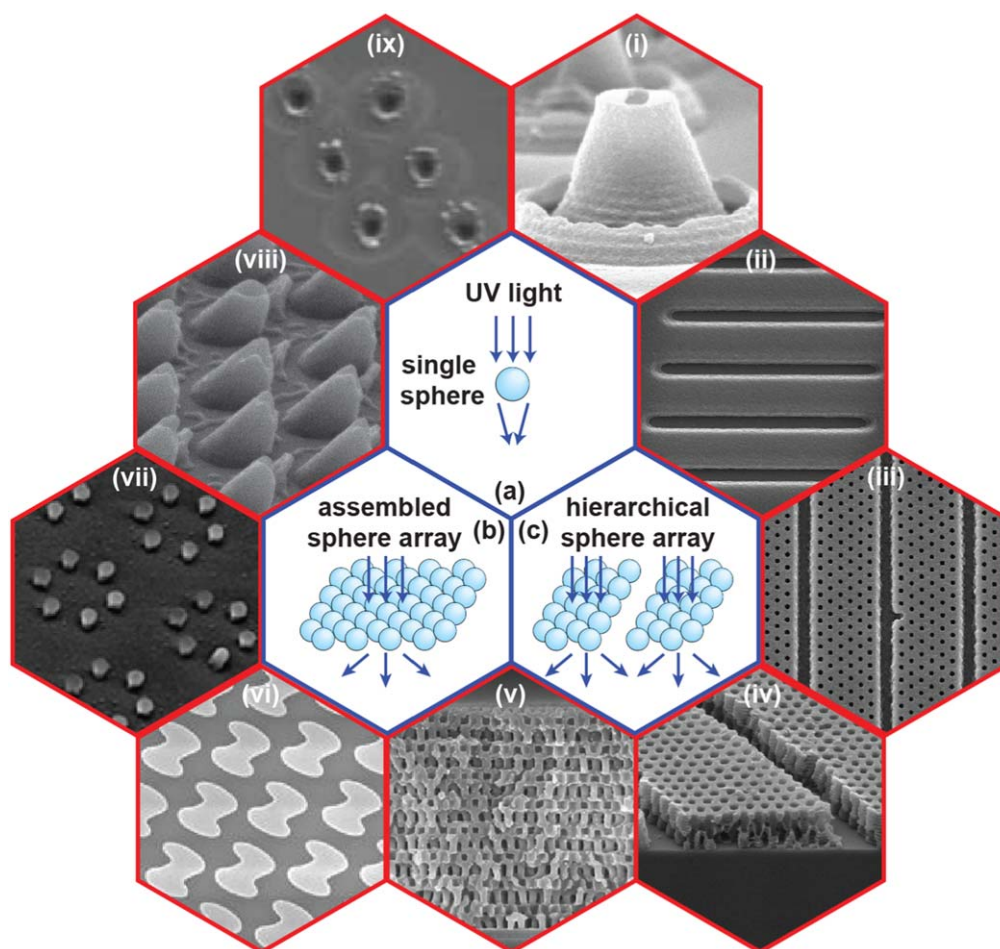


Figure 1. Configurations for near-field 3D nanolithography using light interactions with colloidal nanospheres. Exposure using (a) a single nanosphere, (b) an array of self-assembled spheres, and (c) a hierarchical sphere array. A diverse range of nanostructures can be patterned, including (i) nano-volcano, (ii) parallel trenches, (iii) porous microchannel, (iv) hierarchical structures, (v) 3D photonic crystals, (vi) chiral metamaterials, (vii) hexagonal array of posts, (viii) array of microneedles, and (ix) pores from ablated metal surface. (i) Reproduced with permission [152]. Copyright 2013, American Chemical Society. (ii) Reproduced with permission [151]. Copyright 2017, American Chemical Society. (iii)–(iv) Reproduced with permission [170] with permission of The Royal Society of chemistry (RSC) on behalf of the European Society for Photobiology, the European Photochemistry Association and the RSC. (v) Reproduced with permission [174]. John Wiley & Sons. © 2013 WILEY-VCH Verlag GmbH & Co. KGaA, Weinheim. (vi) Reprinted by permission from Macmillan Publishers Ltd: Scientific Reports [167]. Copyright 2013. (vii) Reproduced with permission [163]. Copyright 2015, Optical Society of America. (viii) Reproduced with permission [154]. John Wiley & Sons. © 2014 WILEY-VCH Verlag GmbH & Co. KGaA, Weinheim. (ix) Reproduced with permission [145]. (2001) © Springer-Verlag 2000). With permission of Springer.

the inverse image of the sphere assembly. Therefore, the patterning versatility of these methods are limited by the initial assembly geometry.

One effective way to introduce patterning versatility is to use the nanospheres for optical lithography, as shown in the schematic in figure 1. The general approach involves illuminating the colloidal assembly with light, which can then create near-field intensity patterns that can be recorded by an underlying photoresist. In this manner, the nanospheres are used as an optical element as opposed to a physical mask, which can create new geometries that are entirely different from the spheres. This approach also adds an element of design, since the patterned structures depend on the illumination conditions in addition to parameters of the colloids. The light interactions with different colloidal assembly, such as (a) single sphere, (b) periodic array, or (c) hierarchical assembly can be studied, as illustrated in figure 1. Some

examples of complex 2D and 3D structures that can be fabricated, including (i) nanovolcanoes, (ii) direct-write trenches, (iii) porous microchannels, (iv) hierarchical structures, (v) 3D photonic crystals (PhC), (vi) chiral metamaterials, (vii) hexagonal posts array, (viii) microneedle array, and (ix) ablated pores on a metal surface. The optical effects that led to the formation of these nanostructures will be discussed in detail.

Harnessing the near-field light interactions with colloidal assembly has a number of key advantages: first, it does not require elaborated precision optics, electronics, and other mechanical components that typically form the foundation of a nanolithography system. Second, high-coherence laser sources are not required since the light interactions harnessed are in the near field. Third, the process is parallel, allowing uniform patterning over large area using a single exposure. Fourth, optical lithography allows accurate structure modeling and inverse design using computational lithography.

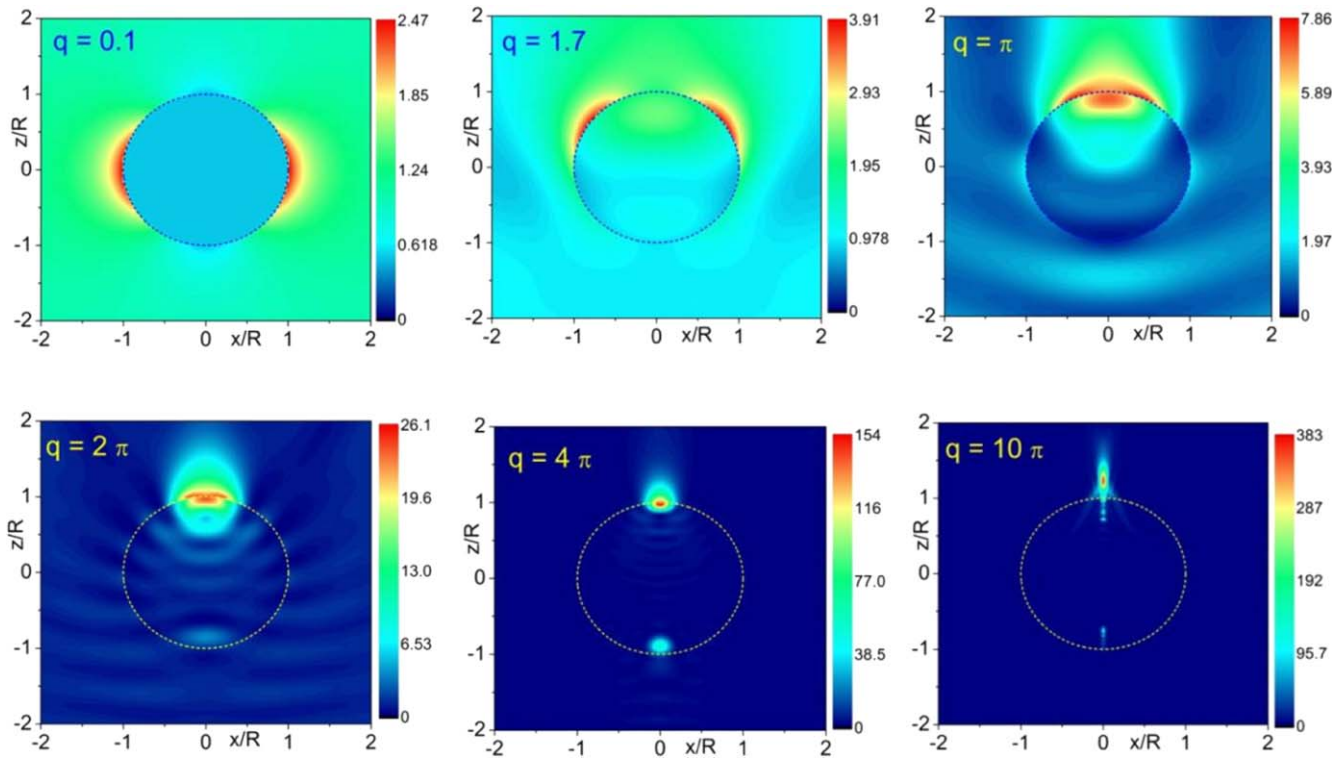


Figure 2. Intensity profiles for a dielectric sphere with various q parameter simulated using Mie theory. The plane wave propagates in the positive z direction. Reproduced with permission [129]. Copyright 2017, Optical Society of America.

Fifth, harnessing the near-field optical effects enables sub-wavelength patterning. Sixth, this new approach is based on a traditional material, namely colloidal nanospheres, where different sizes, materials, geometries are widely available at low cost. Seventh, the process requires simple 2D colloidal assembly that can be obtained with relatively low defects. Lastly, the concept can be applied to other self-assembly systems such as block copolymer, DNA assembly, and non-spherical colloids.

3. Light scattering from a single nanosphere

Colloidal nanospheres is an interesting class of microscale optical elements, which can result in complex optical phenomena when illuminated by plane wave [123–141]. The light scattering field by a sphere is well understood and can be predicted using Mie theory [129]. The scattering depends strongly on the relative ratio of sphere radius (R) to the wavelength (λ), which can be defined by the normalized parameter $q = 2\pi Rn/\lambda$, where n is the refractive index of the medium. The electric field intensity distributions can be plotted for different q values for a dielectric sphere ($n_{sp} = 1.5$) when illuminated by a monochromatic plane wave at normal incident angle, as shown in figure 2. For spheres much smaller than the wavelength, the Rayleigh scattering limit ($R \ll \lambda$) can be observed. Example of scattering in this regime can be seen for $q = 0.1$, where the field pattern resembles an electric dipole. For sphere sizes similar to the wavelength ($R \sim \lambda$), the scattering generates an angular

scattering profile with a strong central intensity lobe, as shown for $q = 2\pi$. Increasing the sphere size further ($R > \lambda$), a pronounced focusing resembling a jet can be observed near the sphere surface of the shadowed side. This has been named a ‘photonic nanojet,’ which can form in the near field of a colloidal element. This optical phenomenon has been well-studied over the last few years, will be examined further in the following sections.

Here two optical regimes can be identified based on the relative ratio of sphere size to the illuminating wavelength. These are (1) the photonic nanojet regime ($R > \lambda$) where the central focal spot is used for direct-write patterning, and (2) the general Mie scattering regime ($R \sim \lambda$) where the angular intensity distribution is employed to pattern more complex geometries. These two optical effects have been studied extensively in literature, and here the emphasis will be on the key parameters to consider in nanolithography.

3.1. Photonic nanojet from illumination of a single nanosphere

Photonic nanojet is the near-field optical focusing of light when the spheres have diameters similar or larger than the illuminating wavelength [123–129]. Such interactions can generate a focused beam with substantial light intensity enhancement, beam waist below the diffraction limit, and propagation length of several wavelengths. Since this effect was observed in early 2000 [129] and the term ‘photonic nanojet’ was adopted in 2004 [123], it has been an active research field [120–141]. In one research direction, efforts have been concentrated in the fundamental understanding and engineering of photonic nanojets in terms of beam waist,

intensity enhancement and propagation length [124–128]. For example, core–shell microspheres have been used to generate long photonic nanojets up to 22 wavelengths long and with enhanced intensity [130, 131]. Other microscale geometries such as cuboid, elliptical microcylinders, and truncated microspheres have also been examined to show increased ability to control the properties of photonic nanojets [132–134]. In another research direction, potential applications of photonic nanojets have been explored. One of the first application is for the detection of objects as small as 5 nm by examining backscattering enhancement [123, 124]. Photonic nanojets have also found applications in low loss waveguide [135], data storage [136], high-resolution microscopy [137, 138], and optical tweezers [139–142]. These applications derive from the benefits of the nanojet having a narrow beam waist below the diffraction limit. More discussion on the formation of photonic nanojets and their properties is extensively described in a recent in-depth review article [129].

The current review is mainly focused on the application of photonic nanojets in nanolithography. This regime has also been referred to as spherical lens lithography in the literature [118]. The key features to be examined are patterning sub-wavelength features, increasing pattern complexity, and extension to 3D nanolithography. Here we will give a brief overview to the optics of photonic nanojet. The important parameters for lithography will be discussed, namely the nanojet width, length, and the intensity enhancement. The nanojet width can be defined as the full width at half maximum (FWHM) of the intensity profile at the focal plane. This parameter defines the patterning resolution, which is approximately $\lambda/3n$ for the nanojet [124–129] and smaller than the far-field Rayleigh diffraction limit of $\lambda/2n$. The nanojet length is also critical, since it describes the depth of focus (DOF) when used in lithography. This is typically in the range of 5λ , which allows patterning of thick resist. Lastly, the enhancement factor governs the peak intensity at the focus, which is important to achieve high exposure dose and reduce patterning time.

Here it is important to examine how these parameters change with the sphere index. For lithography applications the nanojet forms in the underlying resist layer, which typically has an index of $n \sim 1.6$. Therefore, the relative indices of the sphere and the ambient environment must be considered, namely n_{sp}/n [129]. This is similar to applications when the nanosphere is illuminated in a liquid environment for biological trapping and imaging applications [139–142]. The FWHM generally decreases with n_{sp} , which increases the sphere focusing effect. However, increasing n_{sp} also brings the focus towards the sphere surface. At the limit of $n_{sp}/n > 2$, the nanojet focus can be brought within the nanosphere [123, 129]. In the other limit when $n_{sp}/n \sim 1$, no light focusing is possible and the focal plane approaches infinity. On the other hand, the nanojet length has the opposite effect, which decreases to reduce the DOF as n_{sp} is increased [125, 129]. The intensity enhancement is also critical, and generally scales with n_{sp} . This can be attributed to higher focusing, leading to smaller nanojet width and length and

higher intensity at the focus. Another important parameter that controls the shape of the nanojet is the sphere diameter, which can be described by the aforementioned normalized size parameter q . Increasing q generally increases the nanojet length and width, but leads to significant intensity enhancement. The focal plane will also shift towards the sphere surface with increasing q [129]. The exact relationships between these parameters have not been analytically derived and are based on numerical observations, which can offer some design constraints when implementing the photonic nanojet for nanolithography.

3.2. Two-dimensional nanolithography using photonic nanojet from a single nanosphere

The photonic nanojet generated by illumination of a colloidal nanosphere is an excellent candidate for nanolithography since it has sub-diffraction-limit resolution, long DOF, and high intensity enhancement at the focal spot. The simulated intensity profile of a typical nanosphere using finite-difference time-domain (FDTD) method is shown in figure 3(a) [124]. Here a sphere with $3.5 \mu\text{m}$ diameter ($n_{sp} = 1.59$) is illuminated by 400 nm wavelength light in air, generating a photonic nanojet with 190 nm FWHM focus. The nanojet length is around $1 \mu\text{m}$, and the intensity enhancement is around 160. The focal width can be further reduced to 130 nm by using a sphere with $1 \mu\text{m}$, yielding features below the diffraction-limit. The nanojet can then be used for nanolithography to create isolated holes, periodic patterns using sphere arrays, or arbitrary patterns by scanning the nanosphere. It must be noted that since this is a near-field effect and the nanojet is generated within a few wavelengths from the sphere, the material to be patterned needs to be in close proximity. The choice of pattern material is quite versatile, and can be photosensitive materials such as positive or negative photoresist. At high energy doses the nanojet can also be used for focused laser ablation, which can be directly used to pattern the substrates.

Early demonstration of harnessing the photonic nanojet for patterning is in laser ablation of metal surfaces [143–148]. An example is shown in figure 3(b), where an atomic force microscope (AFM) image depicts the depth profile of a hole patterned on an Al surface using photonic nanojet [146]. Here an isolated SiO_2 ($n_{sp} = 1.45$) particle with $0.47 \mu\text{m}$ diameter was illuminated by a single laser pulse with dose of 300 mJ cm^{-2} . This creates a crater-like profile with 5 nm depth and 86 nm diameter. Direct laser ablation of other patterns in different substrates have also been demonstrated [144–148]. The near-field focusing have also been used to clean contaminants on the particle surface [143].

Another advantage of utilizing colloids for nanolithography is their microscale size, which can be readily trapped and manipulated using optical tweezers. This allows the high-precision location control and scanning of the nanosphere, which enables the generated photonic nanojet to pattern arbitrary geometries. This is demonstrated in figure 3(c), where a dual-beam system is illustrated [149]. Here a 532 nm wavelength laser is used to optically trap a PS nanosphere

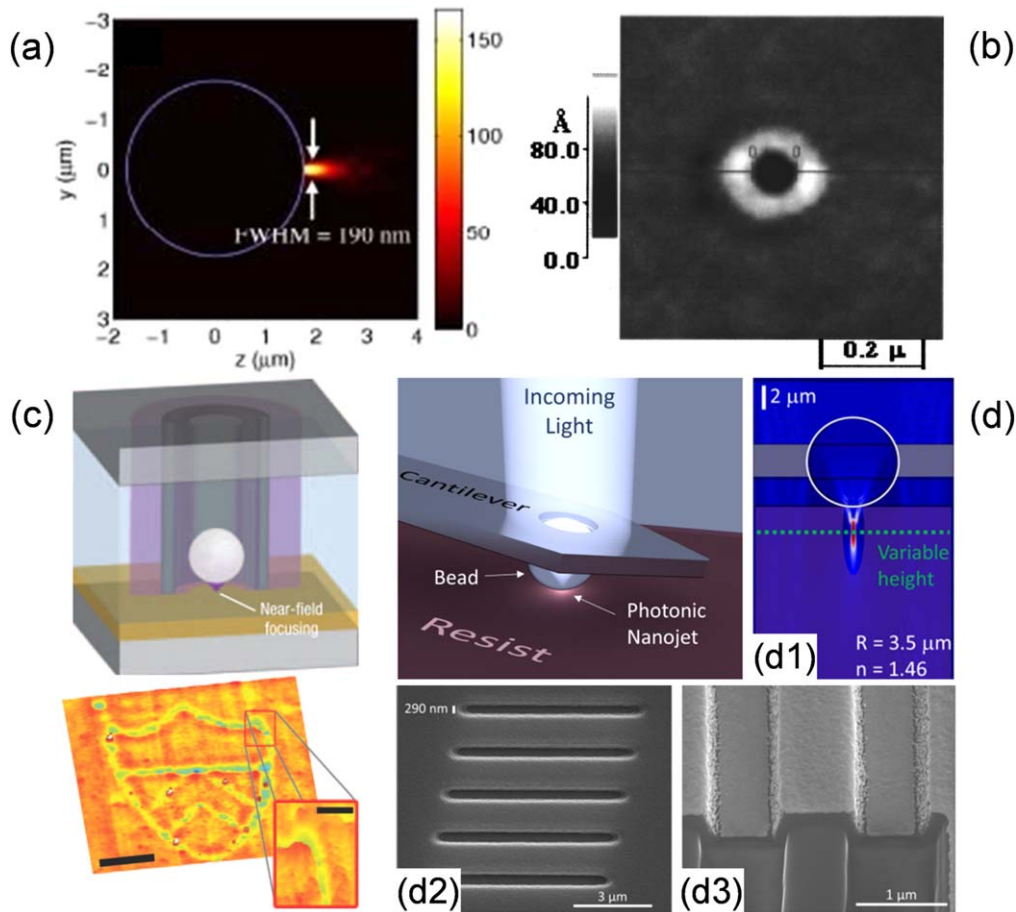


Figure 3. 2D nanopatterning using photonic nanojet generated by a single colloidal particle. (a) Simulated nanojet profile using FDTD methods when a $3.5 \mu\text{m}$ diameter microsphere with index of 1.59 is illuminated with $\lambda = 400 \text{ nm}$. Reproduced with permission [124]. Copyright 2005, Optical Society of America. (b) Measured AFM depth profile of a hole formed on Al surface after illumination of isolated $0.47 \mu\text{m}$ diameter SiO_2 particles. Reproduced with permission [146]. Copyright 2002, with the permission of AIP Publishing. (c) Laser ablation using photonic nanojets generated from a single nanosphere. The particle is trapped by optical tweezer and move in a programmed path to fabricate arbitrary 2D patterns. Reprinted by permission from Macmillan Publishers Ltd: Nature Nanotechnology [149]. Copyright 2008. (d) Scanning probe photonic nanojet lithography where a single particle is attached to a tip of an atomic force microscope. (d1) The focus of the nanojet can create a subwavelength pattern that can be scanned to (d2) pattern 2D features. (d3) Cross-section image of patterned structures. (d) Reproduced with permission [151]. Copyright 2017, American Chemical Society.

($n_{\text{sp}} = 1.62$), which is illuminated by a 355 nm wavelength pulsed laser to generate photonic nanojet for surface ablation. Here the FWHM focus is approximately 100 nm, which is roughly $\sim \lambda/3n$ when considering the index of the water ($n = 1.33$). The nanosphere can be scanned to programmed paths, leading to the patterning of arbitrary patterns as shown in figure 3(c). Some challenges of this approach are that higher resolution is achieved with smaller spheres with diameter of 500 nm, which is more prone to Brownian motion and can reduce pattern precision.

Another technique called scanning probe photonic nanojet lithography has also been introduced to move the photonic nanojet in a programmed path [150, 151]. In this approach, a nanosphere is integrated at the tip of an AFM cantilever, as shown in figure 3(d) [151], which can be raster scanned to pattern arbitrary patterns. In contrast to existing work in AFM-based nanolithography approaches, this technique is non-contact and does not require sharp probes that may wear over time. The simulated intensity pattern using

FDTD method is shown in figure 3(d1), where a tight focus of around 250 nm beam width can be generated from a silica microsphere ($n_{\text{sp}} = 1.46$) with $3.5 \mu\text{m}$ radius. The sphere tip can then be scanned to pattern trenches with 290 nm width, as shown in the top-view and cross-section view scanning electron microscope (SEM) images shown in figures 3(d2), (d3). This technique can be used in a cost-effective manner with the mature position control systems established for AFM.

3.3. 3D nanolithography using scattering from a single nanosphere

While most work on photonic nanojet utilize the central highly focused beam for subwavelength patterning, light scattering in the vicinity of the nanosphere is also interesting to study. Light scattering is a ubiquitous phenomenon and can exist whenever there is a heterogeneity, from molecular to macroscopic scale, in an optical system. In particular, for Mie scattering that occurs when the sphere size is comparable to

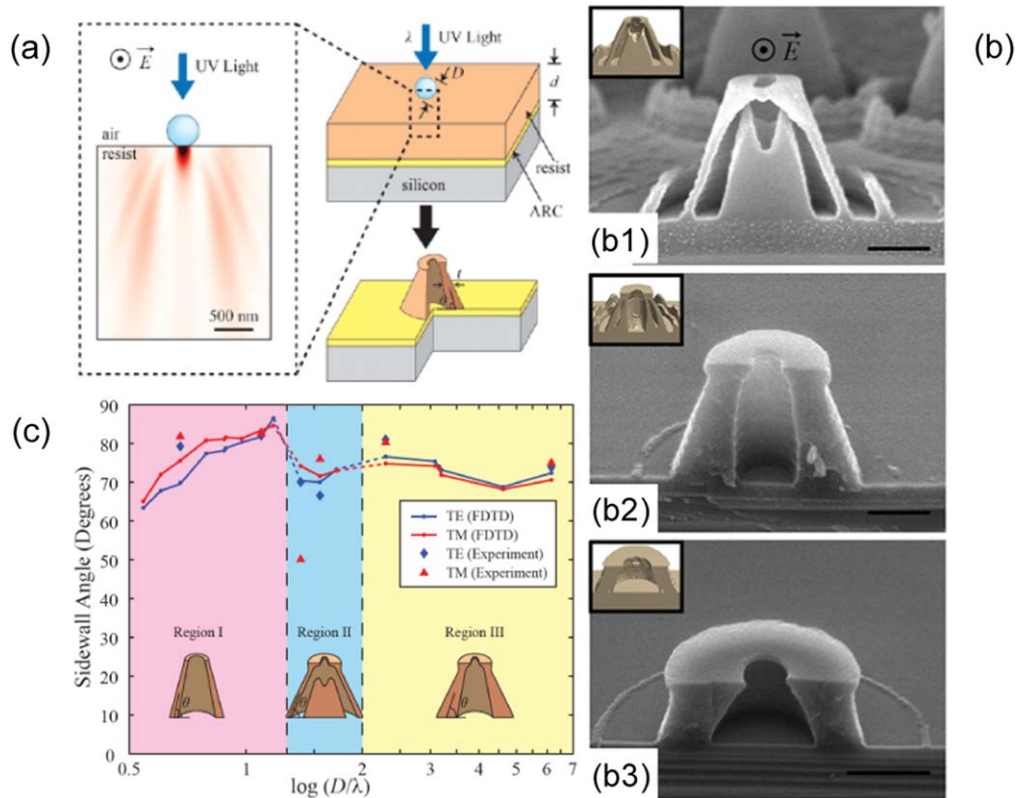


Figure 4. 3D nanopatterning using light scattering from a single nanosphere. (a) Simulated Mie scattering of single particles under normal incidence. (b) Cross-section micrograph of fabricated ‘nano-volcano’ with hollow structures with different exposure parameters. The diameters of PS spheres used for exposure are (b1) 450 nm, (b2) 750 nm, and (b3) 1.9 μm . (c) Three distinct types of ‘nanovolcanoes’ can be achieved by tuning the sphere diameter to wavelength ratio. Reproduced with permission [152]. Copyright 2013, American Chemical Society.

illumination wavelength ($R \sim \lambda$), the angular intensity pattern can be quite complex. This is at the boundary of the typically operating configuration that is used for generating photonic nanojet, which generally employs spheres that are larger than the light wavelength. Under this condition, the light scattering has a directional angular intensity distribution with multiple side lobes in addition to the on-axis nanojet focusing. One example is illustrated in figure 4(a), where a spherical particle with 500 nm diameter is illuminated by 325 nm light [152]. Here the intensity distribution is simulated using FDTD methods, and consists of multiple symmetrical side lobes. Such complex intensity pattern can be readily recorded in photoresist to fabricate 3D nanostructures in single exposures.

Some representative 3D nanostructures are shown in figure 4(b), where the cross-section SEM images depict the patterned conical hollow ‘nano-volcano’ structures [152]. Here figures 4(b1)–(b3) correspond to spheres with diameters of 450 nm, 750 nm, and 1.9 μm , respectively, all of which are illuminated by a HeCd laser with 325 nm wavelength. The 3D structures can be further controlled by the ratio between particle size and wavelength, as shown in figure 4(c), where three types of hollow nanostructures can be identified. An array of nano-volcanos can also be fabricated using a non-close-packed assembly of PS nanospheres. One application of these hollow 3D nanostructures is trapping of nanomaterials,

and a vacuum loading method has been demonstrated to load 50 nm silica particles into the 3D hollow nanostructure [152]. The nano-volcano array can potentially be used as a nanomaterial delivery platform with high spatial resolution, and is the subject of on-going research.

3.4. Oblique and multiple exposures of a single nanosphere

From the previous section, it can be seen that the scattering patterns are in general more complex than the focusing of the main lobe in photonic nanojet. The scattering pattern can be even more complex when the illumination is off axis, as illustrated in the rendering shown in figure 5(a) [153]. Here it can be observed that the angular distribution is highly asymmetric, resulting in structure with spatially varying periodicity. The comparison between normal and oblique exposures can be observed in figures 5(a1)–(a3), where 2D structure fabricated in photoresist are depicted. Here the near-field ripples are symmetric for the normal illumination case, as expected, but are extended with varying density under oblique illumination. The inset diagrams depicted the simulated scattering pattern, which accurately predicts the fabricated planar structures.

Light scattering from oblique illumination of a single nanosphere can also be used to pattern asymmetric 3D nanostructures. This process is shown in figure 5(b), where a thick photoresist layer is used to capture the scattering pattern

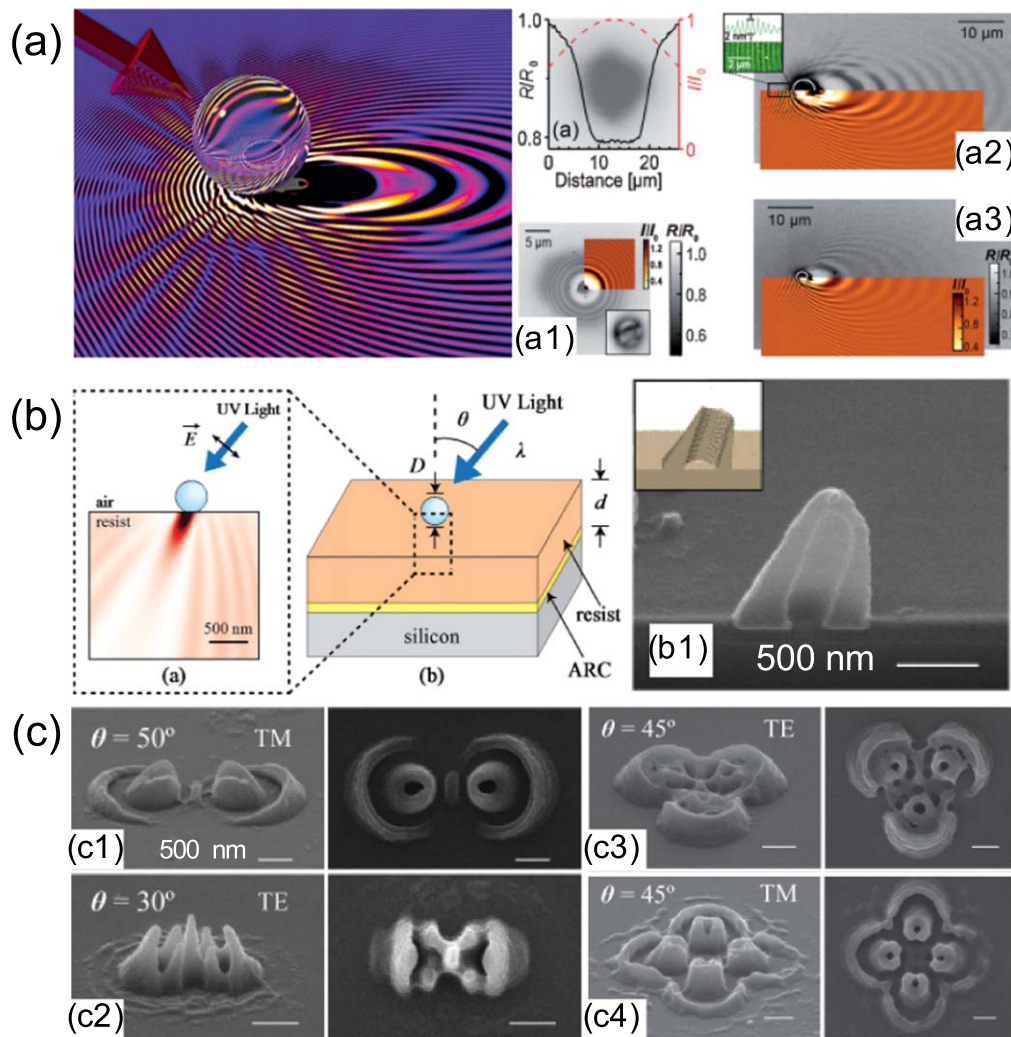


Figure 5. Nanolithography using oblique illumination of single microsphere. (a) Oblique illumination on a large particle can generate ripple-like 2D patterns in photosensitive materials. (a1)–(a3) Patterned planar structures in photoresist using normal and oblique illumination. The simulated scattering intensity pattern are illustrated in the inset diagrams. (a) Reproduced with permission [153]. John Wiley & Sons. Copyright © 2009 Wiley-VCH Verlag GmbH & Co. KGaA, Weinheim. (b) Oblique illumination can also be used for 3D nanolithography. (b1) Fabricated slanted hollow-core structure. (c) 3D nanostructures from multiple incoherent oblique exposures using a single nanosphere. (b), (c) Reproduced with permission [154]. John Wiley & Sons. © 2014 WILEY-VCH Verlag GmbH & Co. KGaA, Weinheim.

[154]. In this manner, a tilted hollow conic structure with a sharp tip can be fabricated, as shown in figure 5(b1). Here a 390 nm diameter nanosphere is illuminated with 325 nm laser with transverse magnetic (TM) polarization at 30° incident angle. The effects of illumination angles and polarization states were also examined, which can result in a diverse range of 3D nanostructures. It was found that TM polarization has a higher impact on the geometry of the 3D nanostructures than the transverse electric polarization due to the larger change in the direction of the electric field direction. This nanolithography process can also be implemented using nanosphere arrays, resulting in an array of asymmetric hollow-core nanostructures that resemble miniature needles, as shown in diagram (viii) of figure 1.

Another way to further increase the pattern complexity is to use multiple off-axis exposures that are either incoherent or coherent. For incoherent illumination, the intensity distribution can be summed by exposing the nanosphere in sequential

fashion without interference effects. This can create 3D nanostructures with higher-order symmetry, as shown in figure 5(c) [154]. Here the sphere is exposed using two, three, and four incoherent exposures, resulting in doublet, triplet, and quadruplets structures as shown in figures 5(c1)–(c4). Different polarization states and incident angles were used, as denoted in the diagrams. The symmetry of these structures is solely determined by the configuration of the sequential illuminations, which adds another degree of control in structure formation. However, incoherent illuminations usually degrade the intensity contrast as more exposures are implemented, leading to shorter nanostructures. This is due to the summation of the background intensity, which is not present in coherent illuminations.

Another approach for off-axis exposures is coherent illuminations, where multiple mutually-coherent light beams are simultaneously incident on the sphere so that interference can occur. A dual-beam exposure configuration is shown in

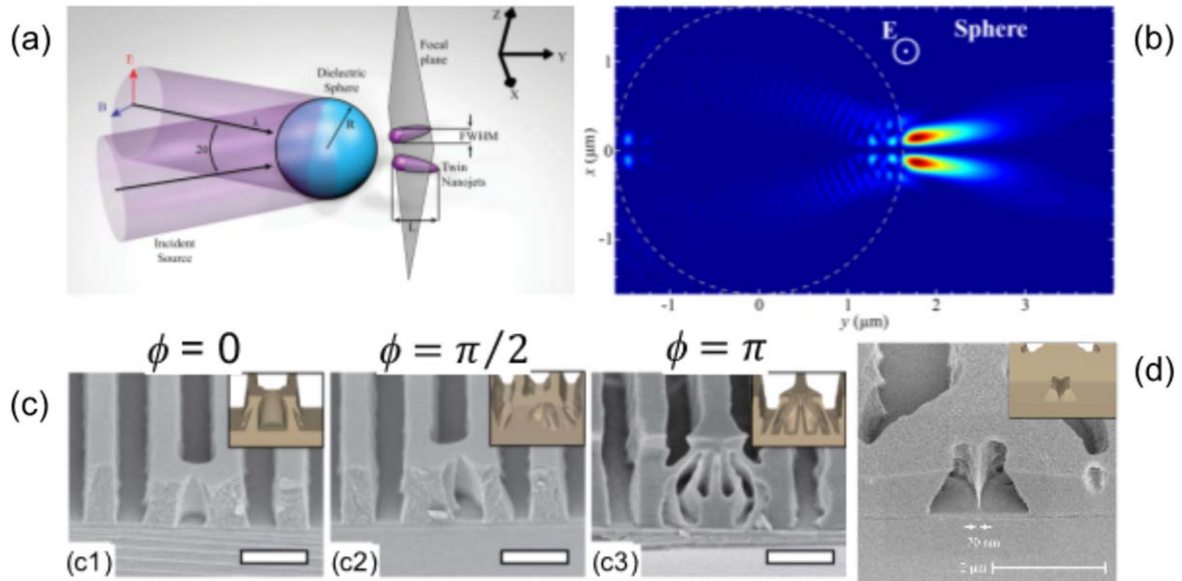


Figure 6. Nanolithography using coherent illumination of a nanosphere. (a) Twin photonic nanojets from two off-axis coherent exposures of a single sphere. (b) Simulated intensity profile from two plane waves ($\lambda = 325$ nm) with π -phase shift and incident angle of $\theta = 5^\circ$. (c) Top-view micrographs of two-beam exposure at 9.4° with (c1) 0, (c2) $\pi/2$, and (c3) π -phase offset. (d) Cross-section micrograph of patterned structure with incident angle at 4.7° . The null at the focal plane can pattern a feature of 70 nm. (a), (b), and (d) Reproduced with permission [155]. Copyright 2018, Institute of Physics. All rights reserved. (c) Reproduced with permission [156]. Copyright 2017, Institute of Physics. All rights reserved.

figure 6(a), where two symmetric photonic nanojets, or ‘twin photonic nanojets,’ can be generated [155]. The resultant twin nanojet can be seen as the coherent summation of two scattering fields, and figure 6(b) depicts the simulated characteristic intensity pattern. Here a $3.25 \mu\text{m}$ diameter sphere ($n_{\text{sp}} = 1.5$) is illuminated with two plane waves ($\lambda = 325$ nm) at 5° incident angle and with relative π -phase shift. The phase difference between the two beams and the incident angles determines the properties of the twin photonic nanojets, which can lead to smaller FWHM focal spot and higher intensity enhancement factor [155]. Such coherent illuminations of a nanosphere can be implemented in a Lloyd’s mirror interferometer, where the twin photonic nanojets can be recorded by photoresist [156]. Figure 6(c) depicts fabricated structures using this approach, where the incident angles are 9.4° and the patterned 3D structures have strong dependence on the relative phase shift between the two beams. The background linear interference pattern serves as a reference to determine the relative phase of the two beams. Here it can be observed that when the beams are in-phase, the two nanojets merge to generate a wider central lobe and results in a single hollow chamber, as shown in figure 6(c1). However, when the beams are out-of-phase, the twin photonic nanojets form and create a two-chamber structure, as shown in figure 6(c3). A more pronounced twin nanojets can be observed when the incident angle is increased to 4.7° , as shown in figure 6(d) [155]. Here it can be seen that the intensity null at the center has high gradient, which allows the patterning of a 70 nm wide structure. Note for this relatively large sphere diameter the typical nanojet width is about 160 nm. This can be attributed to the fact that the coherent illumination of nanospheres results in symmetric photonic nanojets with an intensity null at the center. This creates high

intensity gradient, which has been demonstrated for sub-wavelength patterning and can find other applications in light trapping.

3.5. Limitations, scalability, and other considerations

The nanolithography techniques described in this section rely on the properties of photonic nanojet and angular scattering patterns generated by illumination of a single nanosphere. This approach is solely based on the interactions of light with the nanosphere, which is a simple and cost-effective approach to generate complex subwavelength light intensity patterns. By using different illumination conditions, this can result in subwavelength patterning with feature size around $\lambda/3n$. This technique can also be used for patterning of 3D hollow-core structures with higher-order symmetry, which would not be easy to fabricate using other lithography methods. One significant advantage is that the colloidal element that generates the photonic nanojet is extremely small, and can be readily manipulated in a liquid environment using optical tweezers or in air with traditional mechanical translation stages. This allows the patterning of arbitrary patterns. Note that the technology and hardware involving both of these scanning approaches are relatively mature, and can be readily updated to implement a photonic nanojet direct-write nanolithography system. Multiple nanospheres can also be used to allow parallel writing, which can improve patterning throughput at the expense of higher hardware costs.

However, there are also some limitations associated with this technique that must be considered. First, this is a near-field approach, which means that the colloidal elements must be brought in close proximity to the photoresist layer,

typically in the order of the wavelength. Since the DOF associated with the nanojet length is typically in the order of a few wavelengths, poor height control can lead to time-dependent fluctuations in feature resolution and exposure dose. This might increase the demand for height control sensors and electronics that can increase the fabrication cost. Another method is to use a higher index sphere so that the focal plane is in direct contact, but issues such as sphere damage and contamination would need to be considered. Brownian motion is also a concern for smaller size spheres that reduce feature size, leading to a compromise between pattern resolution and precision.

4. Light diffraction from colloidal assemblies

This section describes using a monolayer of ordered colloidal assembly as an optical element for near-field nanolithography. The self-assembly of nanosphere for direct pattern transfer has been widely studied [116–119], and can form hexagonal close-packed lattice when assembled on a planar surface. In this configuration, the sphere array functions as a periodic phase element, which results in diffraction in the Fresnel regime when illuminated. The key image formation mechanism depends on the sphere size D , which determines the array period $\Lambda = D\sqrt{3}/2$. Two operating regimes can be identified. When the spheres are large ($\Lambda > \lambda$), the periodic spheres generate a parallel array of photonic nanojets. When the spheres are similar to the wavelength ($\Lambda \sim \lambda$), the periodic array can lead to diffraction effects, generating 3D intensity pattern in the near field. This is also known as the Talbot effect [157, 158], a widely studied optical effect that leads to repeating intensity pattern along the optical axis. The key mechanisms and applications for nanolithography will be described in the following sections.

4.1. Focusing by an array of large spheres: parallel photonic nanojets

A powerful method to scale up nanolithography in the photonic nanojet regime is to employ an array of nanospheres. When illuminated, the spheres generate a nanojet array in the underlying resist, enabling parallel patterning that can be potentially scalable for manufacturing. These techniques generally involve spheres that are larger ($\Lambda > \lambda$), so that other diffraction effects are negligible. Here the patterning plane of interest is at the focal plane of the nanojets, which is in close proximity to the sphere surfaces. This leads to the patterning of subwavelength holes and pillars using positive and negative photoresist, respectively. A number of techniques can also be used to increase the patterning versatility of this approach, namely oblique illumination, multiple exposures, and extended light source. These techniques will be described further in the following sections.

4.1.1. Normal illumination of periodic sphere array. A typical nanolithography process using an array of nanospheres is shown in figure 7(a) [159]. Here the spheres are assembled

directly on photoresist to form a hexagonal close-packed lattice. Upon normal illumination, the focused light intensity exposes the underlying photoresist to yield an array of holes in positive-tone photoresist. The structure is patterned by the high intensity focus of the photonic nanojet, as illustrated in the simulated intensity profile using FDTD shown in figure 7(a1). The cross-section SEM image shown in figure 7(a2) depicts a high-resolution profile of the hole patterned using $1\ \mu\text{m}$ silica particle array ($n_{\text{sp}} = 1.45$). The sample was exposed with a dose of $9\ \text{mJ cm}^{-2}$ at a center wavelength of 405 nm using standard photolithography tool, which ensured that only the resist at the focus can be fully exposed. The patterned hole has a diameter of 300 nm and height of 600 nm, showing high aspect ratio. Similarly, an array of posts can be patterned for negative-tone photoresist.

Using this method, different hole array geometry can be designed. By using larger sphere sizes, the lattice spacing between the holes can be controlled. As seen previously when examining the optics of photonic nanojets, spheres with larger sizes do not lead to dramatically larger FWHM beam spots. However, larger hole diameter can be obtained by increasing the exposure dose, since the intensity profile has finite contrast. Figures 7(a3)–(a6) depicts top-view SEM images of patterned hole array with different sphere diameters and exposure dose. The structures in figures 7(a3)–(a4) are patterned using $1\ \mu\text{m}$ diameter silica spheres, while the lower density structures in figures 7(a5)–(a6) are patterned using $2\ \mu\text{m}$ diameter silica spheres. The hole diameters can be independently controlled from 300 to 500 nm by increasing the exposure dose, as illustrated in figures 7(a4) and (a6). Hole arrays with diameters of 300–700 nm and 500–4000 nm have also been demonstrated [159], illustrating the versatility of this patterning process. Similar process uses direct subwavelength patterning of other substrates using high-intensity pulsed lasers [144–148, 160, 161]. More complex unit-cell geometry such as star-shaped patterns can also be patterned using a single normal exposure by employing Mie resonance of the spheres [162].

4.1.2. Off-axis illumination of periodic sphere array. Another method to increase the pattern complexity is through off-axis illumination of the assembled sphere array [163–167]. In this configuration the incident light is at an angle, resulting in a lateral shift of the photonic nanojet focus. FDTD simulations of the intensity profiles produced when a $2\ \mu\text{m}$ diameter sphere is illuminated at different incident angles are shown in figure 7(b) [163]. When the illumination is normal, the nanojet focus is on the optical axis. When the illumination angle is increased to 20° from the optical axis, the focus shifts laterally towards the angle direction. This can lead to additional pattern versatility, which enables the nanojet focal spot to be stepped or scanned by using multiple off-axis exposures. Changing the incident angle can also change the focal plane, which might result in increase of nanojet width [163]. At large incident angles the focus may be shifted out of the resist layer, however, in these cases a lower index particle can be used to increase the focal plane. Note since the

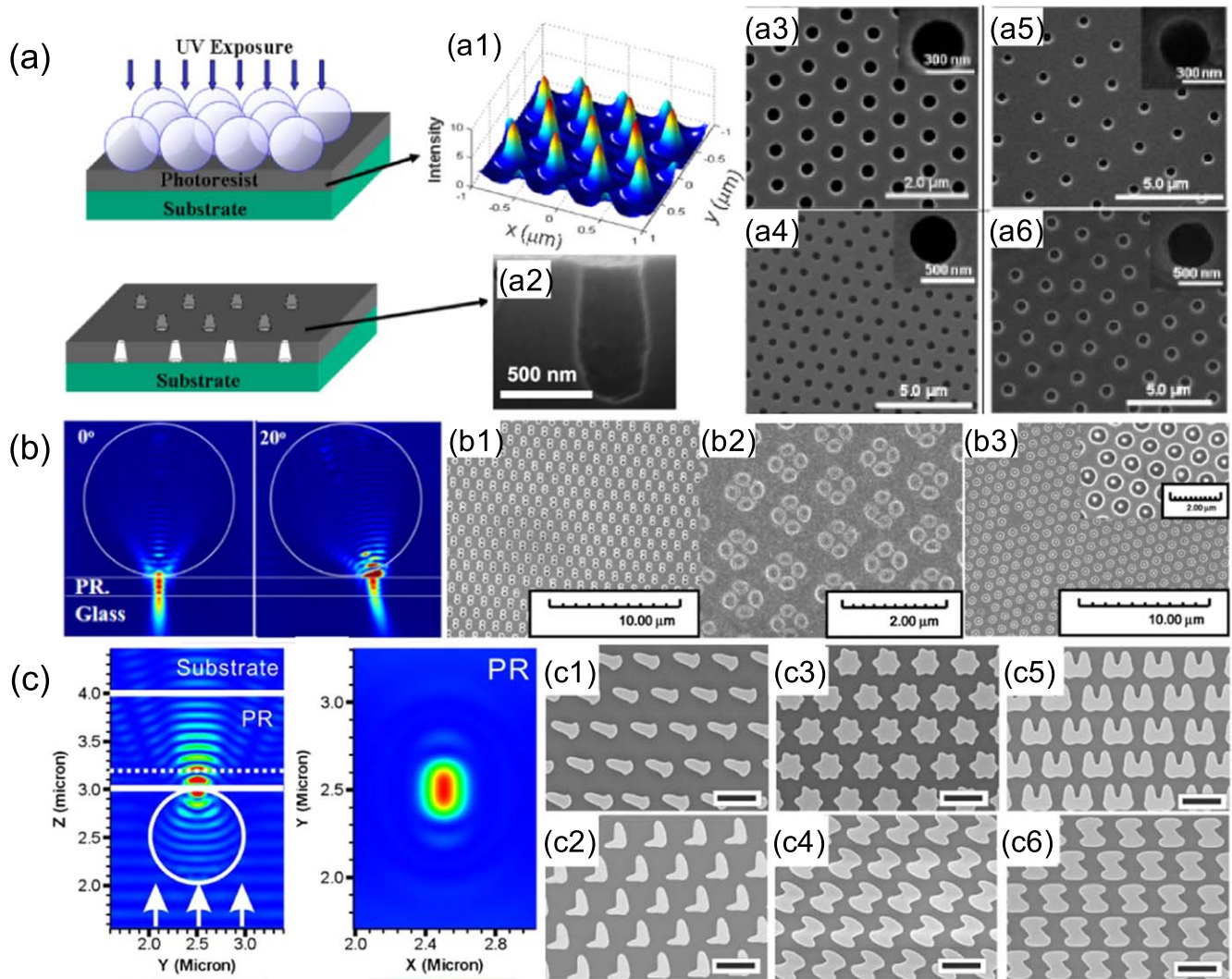


Figure 7. Patterning periodic 2D nanostructures by illuminating an array of nanospheres. (a) Nanospheres assembled on photoresist and exposed using UV laser, generating an array of holes. (a1) The simulated intensity profile in the photoresist. (a2) Cross-section image of hole patterned using silica spheres. (a3)–(a6) Top-view SEM images of patterned resist using different particles and exposure doses. (a) Reproduced with permission [159]. Copyright 2007, Institute of Physics. All rights reserved. (b) Optical effect of off-axis illumination for 0° and 20° . Reproduced with permission [163]. Copyright 2015, Optical Society of America. (b1)–(b3) Fabricated structures with multiple oblique exposures. Reproduced with permission [164]. Copyright 2012, Elsevier. (c) Optical effect of extended source. The resulting intensity pattern is elliptical, with the long-axis aligned to the lamp direction along the y axis. (c1)–(c6) Different unit-cell geometry can be patterned using multiple exposures. Reprinted by permission from Macmillan Publishers Ltd: Scientific Reports [167]. Copyright 2013.

nanojet will also be an array, oblique illumination enables the direct patterning of the unit-cell geometry for the periodic structure.

Multiple exposures at oblique illumination can result in more complex structures, as shown in figures 7(b1)–(b3) [164]. Here hole-pair array was patterned using double exposure of an array of $1\ \mu\text{m}$ PS spheres using $442\ \text{nm}$ wavelength HeCd laser at 45° incident angle, as shown in figure 7(b1). A quad-pair array can be fabricated from two additional exposures, as shown in figure 7(b2). By further increasing the number of exposures, a ring array can be patterned as shown in figure 7(b3). Here the continuous intensity pattern is constructed from a superposition of multiple discrete exposures. Continuous structures can also be fabricated using angular scanning, where the illumination angle is changed over a broad range. It has been demonstrated

to fabricate periodic arrays of straight and curved lines [161]. Other more complex 2D nanostructures can also be patterned by using different exposure conditions [165, 166].

Another method to implement off-axis illumination is to use an extended light source [167]. In previous treatment of the photonic nanojet, the sphere is assumed to be illuminated by a plane wave. However, an extended light source that is not collimated consists of a superposition of plane waves at a wide range of incident angles. This has the effect of elongating the nanojet along the extended source direction, resulting in an elliptical focal spot. This is illustrated in figure 7(c), which depicts the FDTD simulated intensity profile of a $1\ \mu\text{m}$ diameter PS sphere being illuminated by an extended light source that is longer in the y axis. This approach enables single-exposure of periodic arrays of elliptical holes where the alignment of the major axis can

be independently controlled. The ratios of the major to minor axis can be tuned between 1 and 3 by the particle diameter and exposure dose. Using extended light source and multiple exposures at different rotation angles can greatly increase flexibility to design the unit-cell geometry, as illustrated in the range of patterned structure shown in figures 7(c1)–(c6) [167].

4.2. Diffraction from an array of small particles: the Talbot effect

Illumination of a nanosphere array can result in parallel photonic nanojets, which can greatly increase the scalability of this technique. However, additional optical effects can be exploited in the other regime when the sphere diameters are similar to the wavelength of illuminating light. In this case, the 2D monolayer of sphere array behaves as a diffractive element, which diffracts the incident light into discrete orders. These diffraction orders can then interfere in the near field, creating a 3D intensity pattern on the shadow side of the spheres. Known as the Talbot effect [157, 158], this is a near-field diffraction phenomenon created when a periodic optical element is illuminated by a monochromatic source. The intensity pattern repeats along the optical axis, recreating the original image at the primary Talbot plane as well as higher-order images at secondary planes. This optical mechanism and its application in direct patterning of 3D periodic nanostructures will be described in the following sections.

4.2.1. Optics of the Talbot effect. The Talbot effect generates a 3D intensity pattern on the shadow side of a periodic structure when illuminated with a plane wave. The axial period of the intensity distribution is given by the Talbot distance z_t , and can be derived by setting the optical path difference between the 0th and 1st propagation orders in the axial direction to 2π . Consider a structure with lateral period Λ and incident wavelength λ , the normalized Talbot distance is given by [168–170]

$$\frac{z_t}{\Lambda} = \frac{\gamma}{1 - \sqrt{1 - \gamma^2}}.$$

Here $\gamma = \lambda/n\Lambda$ is the normalized length scale parameter, and n is the index of the propagating medium. This expression describes the axial period as a function of the structure period, incident wavelength, and background index. High z_t/Λ can be obtained by having small γ , or $\Lambda \gg \lambda$, where the diffraction angles are close to the optical axis and results in long interference period in the axial direction. Note that the lower limit of $z_t/\Lambda \sim 1$ cannot be achieved to yield structures with equal lateral and axial periods, since no propagating diffraction orders can exist when $\lambda = n\Lambda$.

The Talbot effect can be better interpreted by examining the wave vectors of the propagating modes, as depicted in figure 8. Here a square array of spheres in the space domain and the normalized wave vector in the spatial-frequency domain, are illustrated in figure 8(a). Note for a square lattice the lattice period is the same as the sphere diameter ($\Lambda = D$). Here 8 first-order diffraction modes ($m = 1$) can be observed, corresponding to ± 1 st in the k_x and k_y directions, as well as

the cross orders at 45° . The magnitude of the shortest wave vectors are 1 for $m = 1, 2$ for $m = 2$, and so forth, all located along the k_x and k_y axes. The light circle is also depicted, having a normalized wave vector of $n\Lambda/\lambda$. It can then be observed that when lattice period is smaller than the incident light, or $n\Lambda/\lambda < 1$, the pattern is subwavelength and no propagating orders can exist. When $n\Lambda/\lambda > 1$, the first-order modes are propagating and can interfere in the near field to create a 3D intensity distribution. For $n\Lambda/\lambda > 2$, the higher orders $m \geq 2$ are also included, leading to more complex interference patterns. The fabrication of 3D nanostructures using lithographically patterned phase masks with square lattice has been demonstrated, where larger period of the mask leads to more complex unit-cell geometries [81, 86, 171].

The Talbot effect induced from normal illumination of a monolayer assembly of nanosphere is similar. For self-assembly of nanosphere, the lattice geometry is most commonly hexagonal close packed. The assembly geometry and normalized wave vectors are illustrated in figure 8(b). It can be observed that there are six first-order modes, corresponding to the six-fold symmetry of the hexagonal lattice. Here the noted \vec{k}_1 has magnitude of 1 and is aligned along the k_y axis. Therefore, the necessary condition to create the 3D intensity pattern is $n\Lambda/\lambda > 1$, which can also be expressed in terms of the γ parameter as $\gamma < 1$. For $m = 2$, the shortest wave vector \vec{k}_2 has magnitude $\sqrt{3}$, as denoted in figure 8(b). Similar to the square lattice case, for this order to be propagating $n\Lambda/\lambda > \sqrt{3}$, which yields $\gamma < 1/\sqrt{3}$. Here the Talbot interference pattern will include a secondary axial modulation with a normalized period of $z_t/3$, which is the source of the Talbot sub-planes. By selecting $\gamma < 1/\sqrt{3}$ to allow second-order diffraction, more complex unit-cell geometries can be fabricated. In contrast, a simpler lattice can be fabricated by restricting $\gamma > 1/\sqrt{3}$ so that only first-order diffractions are propagating. The same analysis can be done to show that third and higher-order diffractions occur when $\gamma < 1/\sqrt{7}$, yielding additional Talbot sub-planes.

To examine the accuracy of this analytical model, the z_t is plotted versus the γ parameter for a number of experimental fabrication data, as illustrated in figure 9. The cross-section SEM images of these structures are taken from the literature [168–170], and are shown in later sections. Here the measured data agree well with the analytical equation for the Talbot distance. A numerical plot using FDTD method is also included to further validate the model. Here it can be observed that the normalized z_t exists for $\gamma < 1$, which is the condition for Talbot effect to occur. It is also important to note that the axial and lateral period of the intensity pattern cannot be the same, since $z_t/\lambda = 1$ only when γ approaches 1. For most cases, the axial period would be larger than the lateral period, resulting in taller structures. The different γ parameter regimes are also highlighted, corresponding to $m = 1, 2$, or higher orders that can contribute to more complex unit-cell geometry.

The effect of the Talbot sub-planes on intensity pattern for different γ parameter can be validated using numerical simulation, as shown in figure 10 [169]. Here the intensity

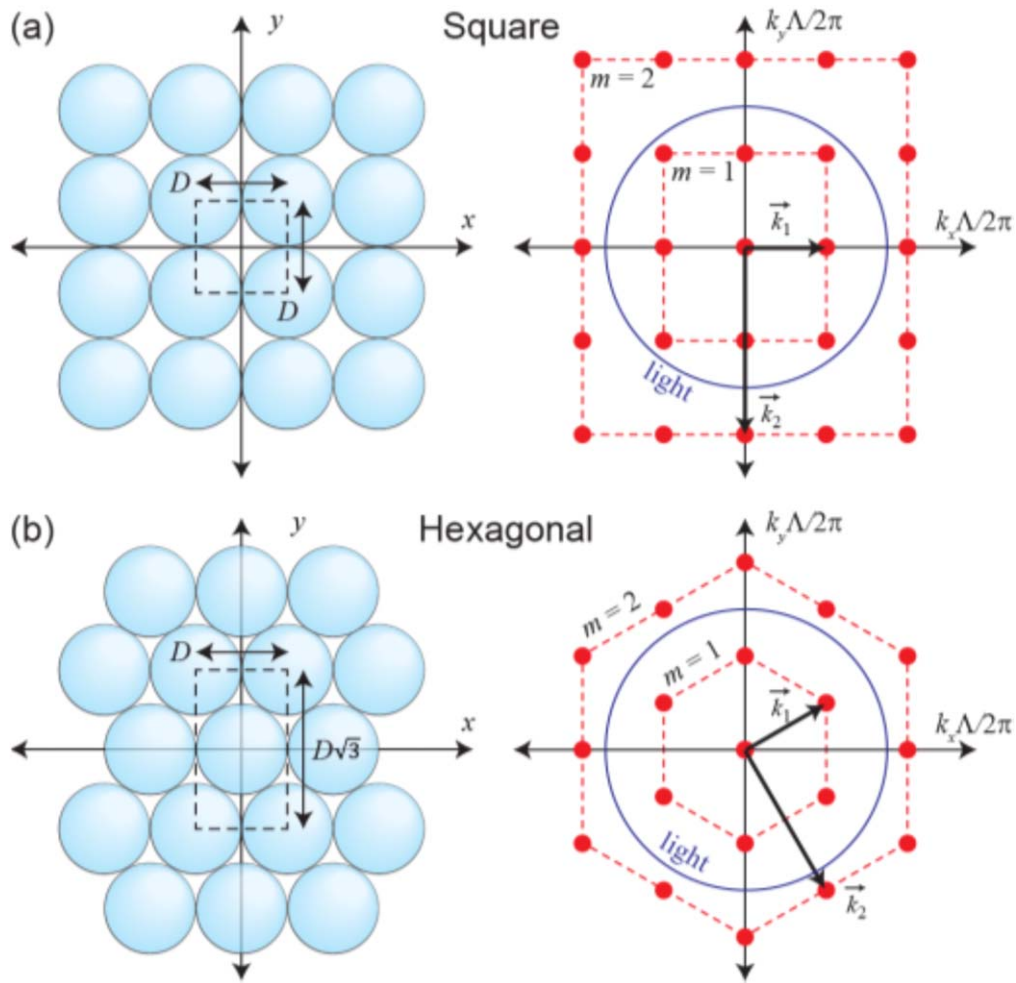


Figure 8. Self-assembled nanosphere array for Talbot effect. Assembly geometry in the space domain and corresponding wave vector in the spatial-frequency domain for (a) a square and (b) a hexagonal lattice.

profiles across the y - z plane (as denoted in figure 8) are simulated using FDTD methods. The unit-cell geometries with normalized z axis are also depicted in the bottom diagram. Here the spheres have index of 1.67 and the wavelength is varied for the same particle diameter to obtain intensity pattern for different γ parameter. It can be observed that at high $\gamma \sim 1$, the intensity pattern is relatively simple with a few repeating images. This is evident in the unit-cell intensity, which consists of only the phase-reversed image. This corresponds to the case where only the $m = 1$ orders are propagating and contributing to the formation of the interference pattern. For $\gamma < 1/\sqrt{3}$, the intensity pattern becomes more complex, where secondary Talbot sub-planes can be identified. This is evident in the unit-cell intensity pattern, where planes with frequency multiplication can be observed. For $\gamma \sim 0.1$, the image is highly complex and multiple higher-order sub-planes can be identified. The unit-cell profile also resembled the typically ‘Talbot carpet’ that depicts a fractal-like pattern with decreasing features [157, 158].

The optical analysis in this section describes the key image formation mechanisms for the Talbot effect, which shows the key advantage of using a sphere array for nanolithography. Among the most critical is versatility, as a

range of 3D intensity pattern from simple to complex can be generated by simply controlling the wavelength to sphere diameter ratio. This can include different period z_t , which can be designed independently of the sphere period. Another powerful tool is to make the use of higher-order diffraction, which can further allow the design of the unit-cell geometry by including multiple Talbot sub-planes.

4.2.2. Patterning of 2D nanostructures using nanosphere array. The 3D Talbot intensity distribution generated by normal illumination of nanosphere array can be an effective method to pattern 2D structures. The unique property in this system is that different 2D unit-cell geometry can be obtained by controlling the distance between the spheres and the photoresist. Effectively, this takes planar slices of the 3D intensity distribution, resulting in different 2D intensity patterns. There is a key difference between this method versus direct replication of the array geometry using additive or subtractive process, or having the photoresist in close proximity of the spheres as in the case of photonic nanojets. In this configuration, the light diffraction from the sphere array results in patterns that are more complex than the geometry of the array. The 3D intensity generated by the Talbot effect can

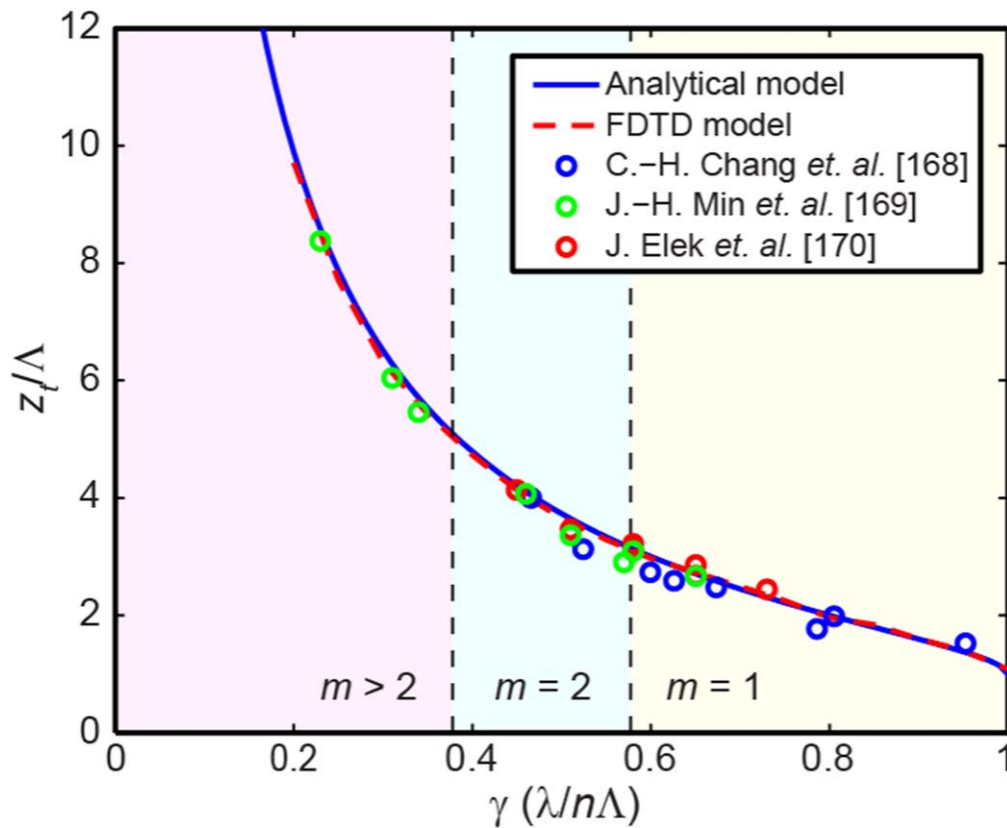


Figure 9. Normalized Talbot distance versus γ parameter simulated using analytical and FDTD models. The experimental data are from [168–170].

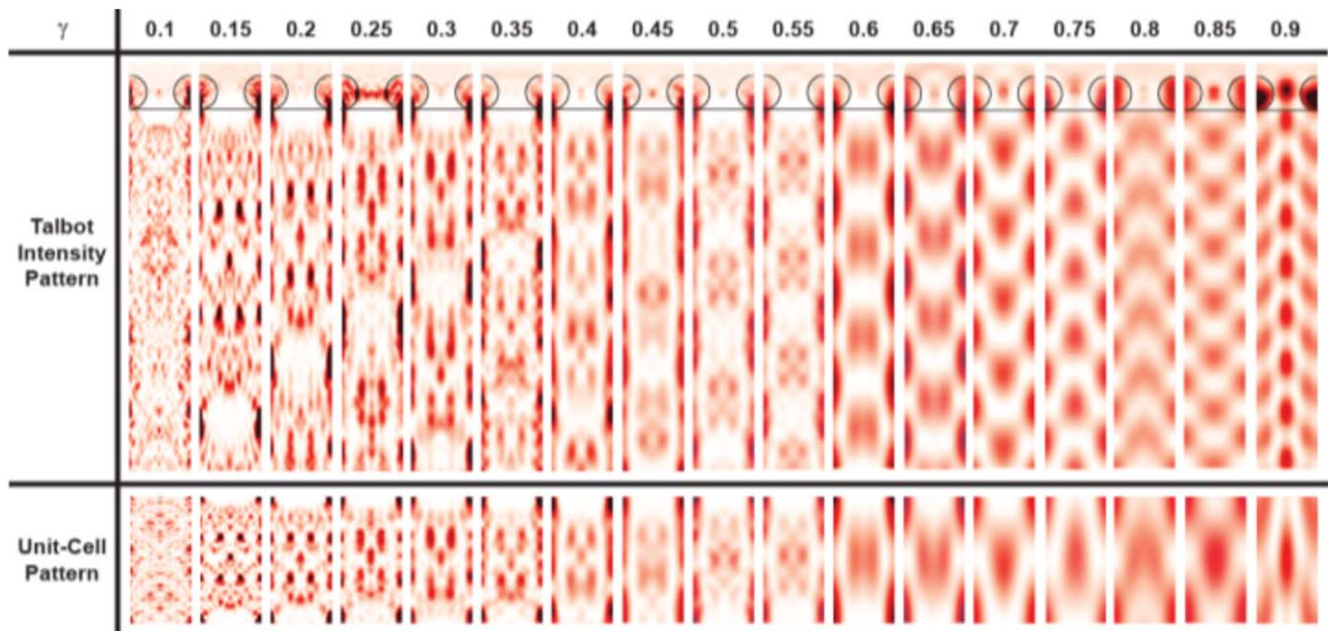


Figure 10. Simulated Talbot intensity pattern in the photoresist layer along the y - z plane for different γ parameter using FDTD methods. The corresponding unit-cell pattern is also shown, illustrating more complex Talbot carpet at low γ due to higher propagation orders. Reproduced with permission [169]. Copyright 2016, Optical Society of America.

also be precisely modeled to control the lithographic process, allowing the design of the fabricated structures.

Early work using this technique was reported by Wu *et al* [172], where microspheres were embedded in a PDMS

substrate for contact microlithography. In this process, an additional thin PDMS layer is used to control the distance between the PS spheres and photoresist, as illustrated in figure 11(a). By controlling the PDMS spacer layer, a range

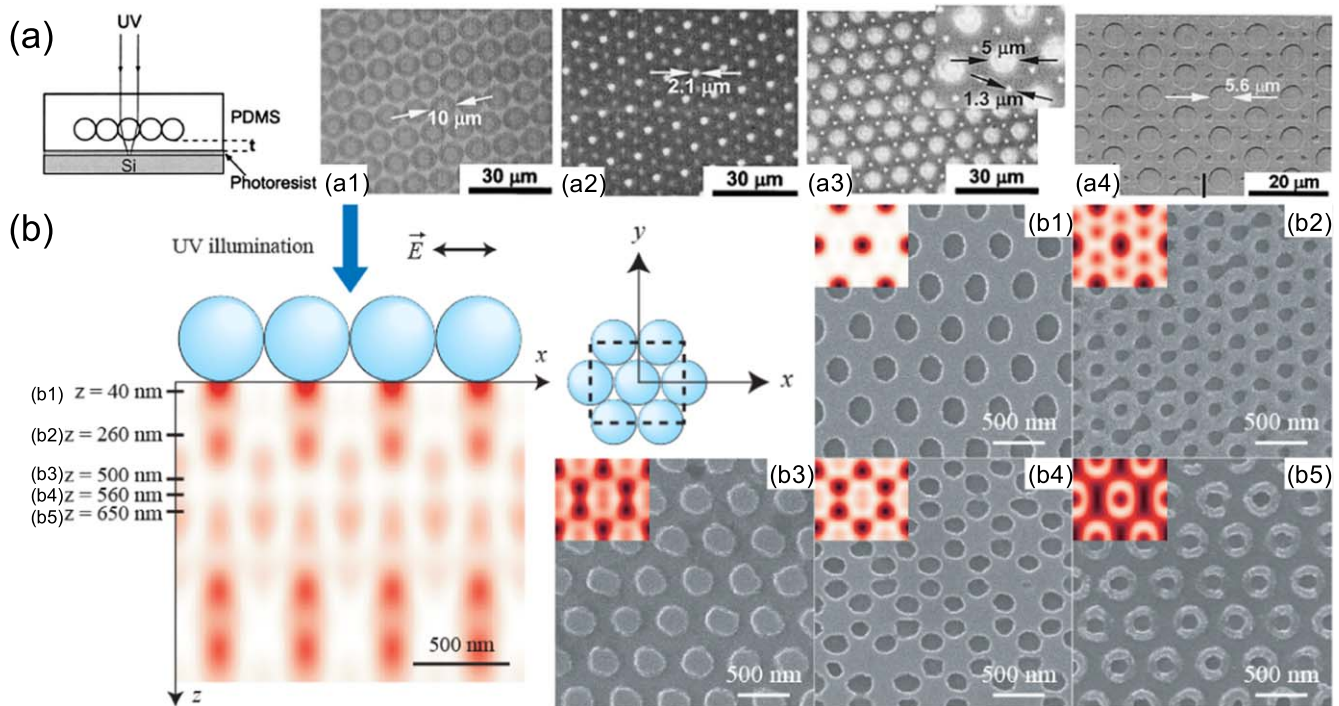


Figure 11. Designing unit-cell geometry of 2D patterns using Talbot effect. (a) A finite gap can be introduced to control the distance between the spheres and photoresist plane. (a1) Optical micrograph of self-assembled $10\ \mu\text{m}$ diameter PS spheres. Observed optical images produced by the spheres with distances of (a2) $4.6\ \mu\text{m}$ and (a3) $0\ \mu\text{m}$ from the focal plane, respectively. (a4) Patterned photoresist corresponding to the position shown in (a3). Reproduced with permission [172], Optical Society of America. Copyright 2002.. (b) Near-field slicing using $450\ \text{nm}$ diameter PS nanospheres, overlaid with intensity profile simulated using FDTD. A thin photoresist layer is placed at the z -planes noted using a HSQ spacer layer, resulting in the fabricated results shown in (b1)–(b5). The inset diagrams are simulated intensity profile for each plane. Reproduced with permission [168]. Copyright 2011, American Chemical Society.

of structures can be patterned when the mask is illuminated with UV light. The optical micrograph of the mask with embedded $10\ \mu\text{m}$ diameter PS spheres are shown in figure 11(a1). When the spacer distance is small, the pattern structure is an array of holes, similar to the results in the photonic nanojet regime. As the distance increases, however, holes with smaller features start to form at the interstitial sites, as shown in the microscope image of the light pattern in figure 11(a2), where the distance is $4.6\ \mu\text{m}$. The smaller holes are the result of the spatial-frequency multiplication effect from the higher-order Talbot sub-planes, resulting in $2.1\ \mu\text{m}$ diameter features. This can be used to pattern structures with smaller feature size than the sphere diameter, as shown in the microscope image of the light pattern and top-view SEM of patterned structures in figures 11(a3) and (a4), respectively. Here the patterned holes have diameters down to $1.3\ \mu\text{m}$, which is smaller than the sphere diameter of $10\ \mu\text{m}$. It is important to note that embedding the PS spheres ($n_{\text{sp}} = 1.6$) within PDMS ($n = 1.4$) reduces the refractive index contrast, which is critical to induce phase modulation to create the Talbot effect. Spheres with index lower than carrier substrate can also be used, which results in defocusing of light and can lead to different patterns [172, 173]. This approach is favorable for scale-up production, since the sphere-embedded PDMS mask can be reused. More discussion regarding scalability and manufacturing will be described in section 4.4.

More recent work aims to assemble the sphere array directly on a photoresist stack that includes a transparent space layer for nanolithography [168]. This process involves using a spin-on oxide such as hydrogen silsesquioxane (HSQ), which can be spincoated on top of the photoresist and temperature treated to form silicon oxide. This approach is attractive in that the array of self-assembled nanospheres functions as the microscale optical phase element to diffract light and no physical mask is needed. This approach has a number of advantages, including higher index contrast of the spheres with ambient air. This can result in stronger diffraction amplitudes and contribute to higher contrast of the Talbot intensity pattern in the near field.

The fabrication process of this approach is illustrated in figure 11(b), where an array of $450\ \text{nm}$ PS nanosphere array is under normal illumination ($\lambda = 325\ \text{nm}$) [168]. The near-field intensity pattern as a result of the Talbot effect is simulated using FDTD method, as overlaid in the diagram. The HSQ spacer can then be controlled from 40 to $650\ \text{nm}$, resulting in a wide range of photoresist structure with different unit-cell geometry, as shown in figures 11(b1)–(b5). For $z = 40\ \text{nm}$, a hexagonal array of holes similar to the photonic nanojet regime can be obtained, as shown in figure 11(b1). For $z = 260\ \text{nm}$, another set of holes associated with the Talbot sub-planes appears to increase the spatial frequency of the pattern, as shown in figure 11(b2). For $z = 540\ \text{nm}$, the pattern is the phase-reversed image of the sphere array, or an array of pillars, as shown in figure 11(b3).

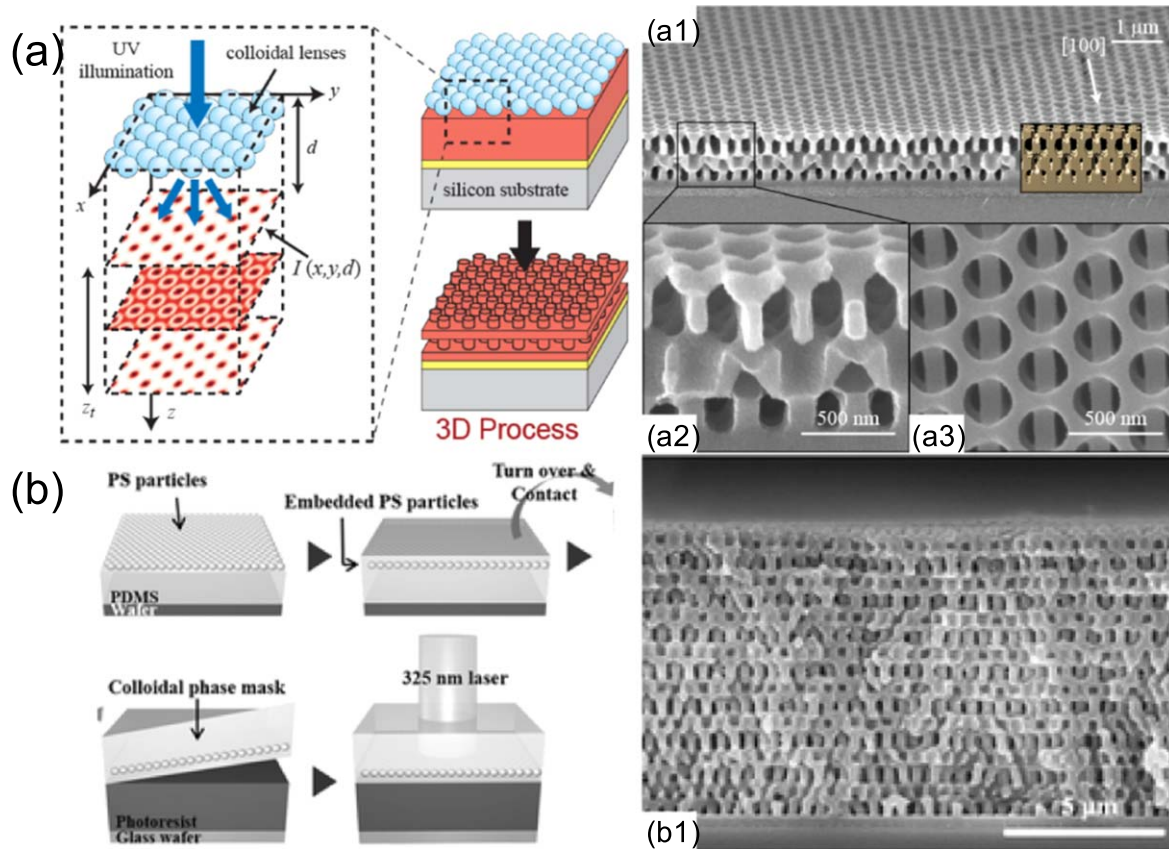


Figure 12. Patterning 3D nanostructures using the Talbot effect. (a) The nanosphere array is assembled directly on a thick photoresist layer. (a1)–(a3) SEM images of fabricated nanostructure in photoresist using 350 nm nanospheres with $\lambda = 351$ nm. Reproduced with permission [168]. Copyright 2011, American Chemical Society. (b) PS nanospheres can also be embedded in a conformal PDMS mask, which under normal illumination can pattern (b1) 3D periodic nanostructures. Reproduced with permission [174] John Wiley & Sons. © 2013 WILEY-VCH Verlag GmbH & Co. KGaA, Weinheim.

For $z = 560$ nm, this is another Talbot sub-plane where the intensity pattern at the interstitial sites can be enhanced, as shown in figure 11(b4). For $z = 650$ nm, a hexagonal array of rings can be patterned, as shown in figure 11(b5). Using the near-field Talbot effect is a powerful technique, where the same sphere and exposure wavelength can lead to different 2D patterns by simply altering the distance between the photoresist and the spheres.

4.2.3. Patterning of 3D nanostructures using nanosphere array. In addition to fabricating 2D patterns with different unit-cell geometry, the intensity distribution generated by the Talbot effect can also be used to directly pattern periodic 3D nanostructures. In this approach, as shown in figure 12(a), the nanosphere array is assembled directly on a thick photoresist layer [168]. The spheres array can then be illuminated with UV light, generating the 3D intensity pattern that is then recorded by the underlying photoresist. This approach has a number of key advantages. First, this near-field light diffraction creates a volumetric intensity distribution, allowing the patterning of periodic 3D nanostructures with a single exposure. Second, as described in section 4.2.1, the intensity pattern is well-described by the Talbot effect and can be precisely designed by controlling the γ parameter. Third,

direct assembly on the photoresist ensures close contact, which leads to uniform patterning of the structures over large areas.

Experimental demonstration of this approach is illustrated in figure 12(a1), where SEM images of the patterned periodic 3D structures are depicted. Here an array of 350 nm diameter PS nanospheres was exposed using a laser with 351 nm wavelength. This results in a γ parameter of 0.67 and calculated $z_t = 780$ nm. Figure 12(a2) depicts a higher magnification cross-section, and the structure can be seen to be periodic in all three directions with measured $z_t = 750$ nm. The smaller experimental value can be attributed to the out-of-plane sagging of the porous structure after development. The top-view image in figure 12(a3) reveals layers that are consistent with those predicted at a single distance to the spheres. Recent work has also demonstrated that different γ parameter can be obtained by using different sphere diameters and exposure wavelengths, which can lead to different z_t and unit-cell geometry [168–170]. Note there is also a polarization effect, and the electric field is aligned with the [100] direction for the structure depicted in figure 12(a1). For non-polarized light the patterned structures would reflect a six-fold symmetry corresponding to the sphere array [168]. Note this method does not require the use of a coherent light source,

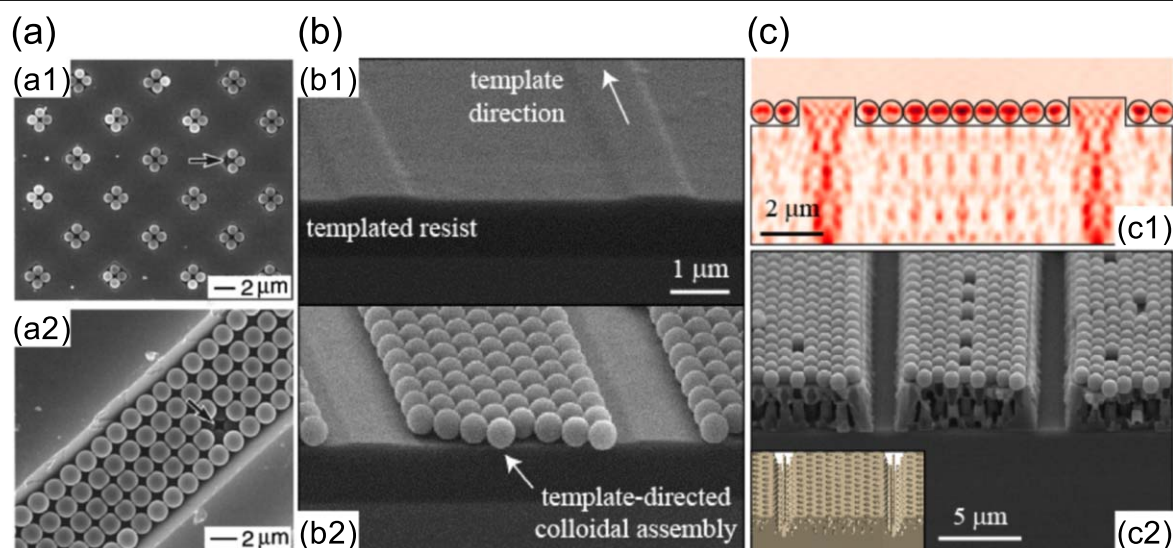


Figure 13. Patterning of hierarchical nanostructures using template-directed colloidal assembly. (a) Assembly of nanospheres using silicon substrate with (a1) an array of square holes and (a2) trench. Reproduced with permission [106]. Copyright 2001, American Chemical Society. (b) Sample preparation for hierarchical patterning using (b1) photoresist with surface relief grating that can be used to (b2) selectively assemble nanospheres. (c) Patterning of 3D hierarchical nanostructures. (c1) Simulated intensity pattern using FDTD and (c2) cross-section SEM image of fabricated microchannels with 3D nanostructures. (b), (c) Reproduced with permission [170] with permission of The Royal Society of chemistry (RSC) on behalf of the European Society for Photobiology, the European Photochemistry Association and the RSC.

and a Hg lamp with narrowband filter at 405 nm has been used to pattern 3D periodic nanostructures.

In addition to direct assembly of the sphere array on the photoresist, the spheres can also be embedded within a PDMS substrate for contact 3D lithography [174–181]. This is illustrated in figure 12(b), where PS spheres are assembled on a layer of PDMS carrier [174]. Another thin layer of PDMS can then be used to fully contain the spheres, resulting in a PDMS mask with embedded array of PS nanospheres. This colloidal phase mask can then be brought in direct contact with thick photoresist, which can be patterned with 3D periodic nanostructures when illuminated. An example of the patterned structure is shown in figure 12(b1), where the SU-8 nanostructure is periodic in all three directions. Using different sphere diameters, nanostructures with different lattice geometries can be patterned. This approach has several key advantages, the most attractive being that the colloidal phase mask can be reused repeatedly. This is especially attractive for scale-up manufacturing, which will be described further in section 4.4.

4.3. Hierarchical array using template-directed self-assembly

In previous section, we describe the patterning of 3D periodic nanostructures using a uniform array of nanospheres. In those experiments that key is to get large-area patterning of the structures, which can then be used for photonics, ordered cellular solids, and other applications of nanostructured materials. However, for device applications it may not be desirable to have uniform nanostructures, but instead only in selected regions. Examples include photonic waveguides with 3D PhCs [107], or microfluidic channels [40, 41], and

hierarchical electrodes for energy storage [43, 44]. It is then important to pattern microscale strips that consists of 3D periodic nanostructures, which results in a hierarchical array.

The key to enabling hierarchical patterning is to control the self-assembly of the nanospheres to selected regions. This can be achieved by using a physical template, which is also known as template-directed self-assembly, a powerful technique in ‘bottom-up’ nanofabrication [106–109]. An early example of this approach is illustrated in figure 13(a), where silicon templates are used to trapped nanospheres in a square array of holes or a long trench [106]. Using this concept, a physical template can also be created on the photoresist surface, which can then direct the assembly of the spheres to regions where the 3D nanostructures are desired, as shown in figure 13(b). Using solvent-assisted soft lithography, a shallow surface topography was created on the photoresist layer [170], as shown in figure 13(b1). This process is performed at low temperature, leaving the photosensitivity of the resist unchanged. Note the template geometry is relatively large with microscale features, and can be patterned into arbitrary shape using standard microlithography techniques.

The photoresist template can then be used to direct the self-assembly of the nanospheres to only the trench areas, as illustrated in figure 13(b2) [170]. Upon normal illumination, the assembled nanospheres create 3D intensity pattern as governed by the Talbot effect only in regions where there are colloidal assembly, as illustrated in figure 13(c). The intensity pattern can be simulated using FDTD method and is shown in figure 13(c1). Here it can be observed that in regions with spheres, 3D patterns similar to those from a uniform sphere array can be generated. However, some edge diffraction effects

can be observed, where the fields below the last sphere are not perfectly periodic. For the regions without the spheres, the intensity pattern is much higher and does not form obvious 3D patterns. The fabricated structure for the corresponding case is shown in figure 13(c2). Here the spheres remained after development, precisely marking the regions with the assembly. It can be observed that 3D periodic nanostructures are patterned under the sphere array, and the resist is fully exposed in regions without spheres. This result demonstrates that using template-directed assembly, 3D nanostructures can be patterned in prescribed regions. This enables the formation of microscale patterns of periodic 3D nanostructures, which can lead to applications in photonic circuits and porous microchannels.

4.4. Limitations, scalability, and other considerations

The illumination of an array of nanospheres, through either the photonic nanojet regime or the Talbot effect, is an effective tool for nanolithography. This approach has a number of advantages, the key being that the intensity pattern is formed solely through the interactions between light and the nanosphere, greatly reducing hardware complexity. The pattern geometry can also be precisely designed by controlling the ratio between the sphere diameter and incident wavelength, resulting in significantly more complex patterns than the sphere array used. In addition, this light-colloidal interaction is scalable to smaller wavelength, which can potentially allow 3D pattern of sub-100 nm period structures using EUV radiation.

Another important aspect is the selection of the illumination source for this method. Since the optical effect is induced by diffraction from a periodic structure, a light source with high coherence is not required. However, it is important that exposure light be as monochromatic as possible, since a broad wavelength band can lead to a wide range of Talbot distances. This can reduce the intensity contrast and degrade process latitude. Therefore, a narrow bandpass filter should be utilized for exposure using a broadband source such as arc lamps. High optical power is also not required since the background vibration is not a significant issue. This can be attributed to the fact that the spheres and photoresist surface are in direct contact and the resulting intensity profile is spatially phase-locked. Other low-coherence, non-polarized sources such as laser diodes have also demonstrated to work well, greatly reducing the hardware costs for this approach.

However, there are a number of key limitations that must be considered. First the formation of high-quality structures, especially for the Talbot effect case, requires spheres that are ordered in a periodic array. Therefore, any assembly defects such as point vacancy, grain boundary, or aggregation can lead to poor exposure. Various studies have been performed to prescribe process conditions to reduce defect density, including using monodispersed nanospheres that have narrow size distribution and optimal assembly conditions. Second, when using nanosphere array as a phase element, the sphere height and period are coupled. This leads to limited degrees of freedom in designing the periodic modulation, which can result in fewer unit-cell geometry and lower exposure contrast

when compared with using a lithographically patterned 2D phase mask [86].

However, one of the greatest advantages of this approach is the low process and equipment cost, which poses great potential for scalable nanomanufacturing. Direct assembly of the nanosphere on the photoresist surface is attractive for many reasons. Namely it eliminates the need for a 'physical mask,' and the substrates are illuminated with the self-assembled elements. To improve scalability, various assembly scheme can be considered [115]. A promising method is convective assembly [101, 102], where colloidal nanospheres in the suspension withdraw to the dry edge by the flux to compensate for the evaporated solvent. Spincoating is also an effective method, and have demonstrated full-wafer assembly with the number of assembly layer controlled by the spin speed [103]. Langmuir-Blodgett (LB) method can also be used to assemble colloidal elements on an air-water interface and then transferred to a carrier substrate [104]. The compression process of LB method can be implemented by a moving carrier fluid, leading to a continuous roll-to-roll colloidal assembly system [105]. One limitation with these techniques is that since self-assembly is an energy balance system, it can be extremely difficult to achieve defect-free assembly. A possible solution would be the integration of template-directed self-assembly techniques in the manufacturing chain, since it has been demonstrated as a viable technique to reduce defect density [109]. However, this could require extra capital to design and manufacture the templates.

Another way to improve scalability is to embed the nanospheres within a conformable, transparent polymer substrate such as PDMS [172–181]. The substrate then serve as a carrier medium, which can be cleaned and reused repeatedly. The spheres can either be used directly as the phase element, or further micromachining such as etching can be performed to transfer the pattern directly into the substrate [180, 181]. This approach has been demonstrated for patterning of both 2D and 3D nanostructures. However, one drawback of this approach is that the index contrast between the spheres and substrate material is small, which reduces the phase-shift induced by the element [172–174]. This can potentially lead to lower exposure contrast for some particle diameters. In addition, there may be close contact issues such as in-plane or out-of-plane mask distortion and strain gradients that can lead to birefringent effects. Other issues such as particle contaminants and mask wear must also be mitigated.

5. Applications

Harnessing the light interactions with nanospheres can lead to a wealth of 2D and 3D nanostructures that would otherwise be prohibitively expensive to fabricate. More importantly, the patterned geometry can be significantly more complicated than those that can be obtained using traditional micromachining of nanosphere assemblies. Having periodicity in two or three-dimensions and complex unit-cell geometries, these structures can find many applications in nanophotonics, nanoarchitected materials, and micro/nanofluidics. Here we

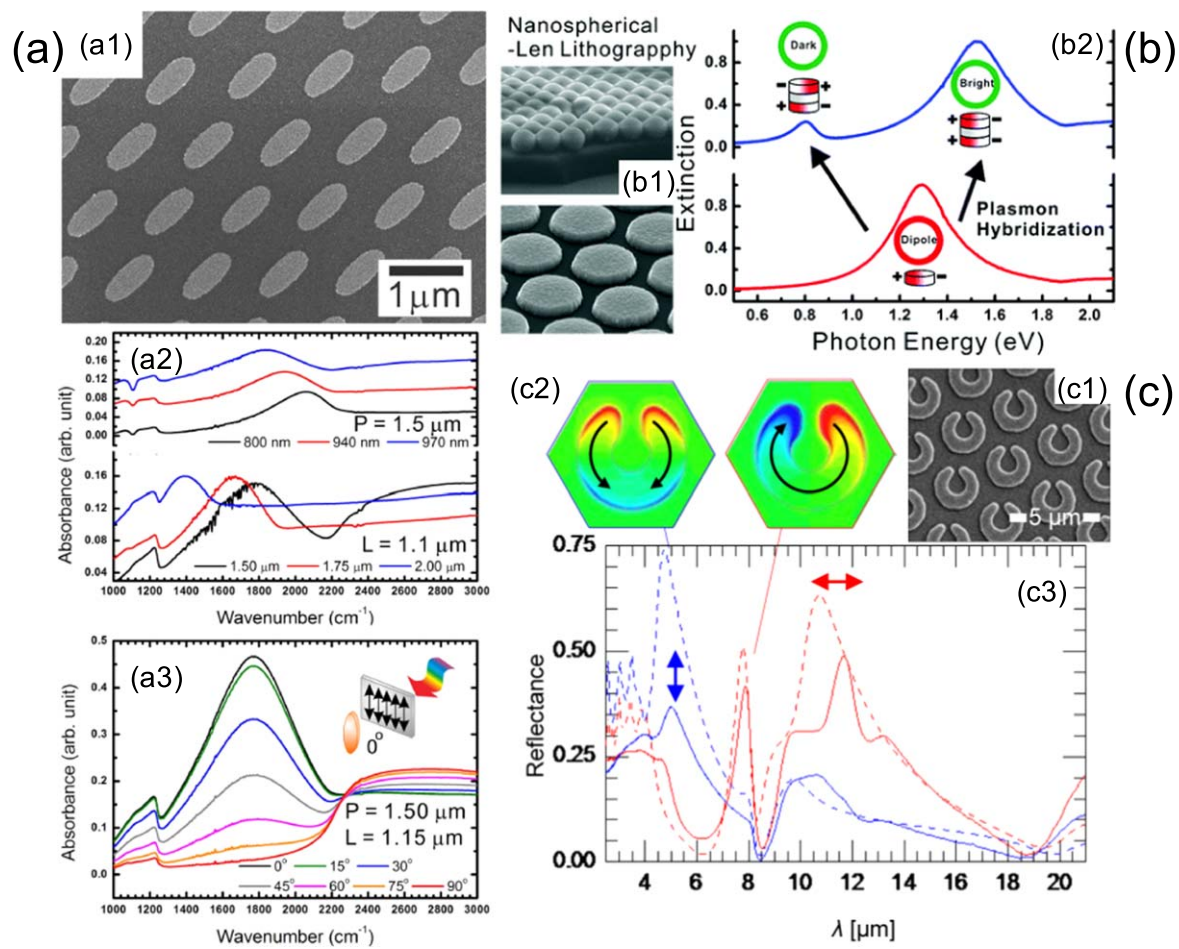


Figure 14. Planar plasmonic elements fabricated using an array of nanospheres. (a) Using illumination from an extended UV source, (a1) an array of Au nanoellipses can be patterned. (a2) FTIR spectra of Au nanoellipse arrays with varying long-axis length and array period. (a3) Polarization-dependent FTIR spectra of nanoellipse arrays (long-axis length of $1.15 \mu\text{m}$ and period of $1.5 \mu\text{m}$). Reprinted by permission from Macmillan Publishers Ltd: Scientific Reports [167], Copyright 2013. (b) Metal–insulator–metal (MIM) nanodisk array with hybridized plasmon modes. Reproduced with permission [182]. Copyright 2012, American Chemical Society. (c) Off-axis illumination of nanosphere arrays can be used to pattern (c1) split-ring resonators. (c2) The simulated field distribution of resonant modes for light polarized in the vertical (left) and horizontal (right) directions. (c3) The reflectance spectra indicate the resonant modes are at $\lambda = 4.8$ and $7.8 \mu\text{m}$. Reproduced with permission [187]. Copyright 2017, Optical Society of America.

will highlight a few applications in plasmonics and metamaterials, light-extraction photonic nanostructures for solid-state lighting, and multifunctional nanolattice materials.

5.1. Plasmonics

Plasmonic devices are based on the interactions of light at a metal–dielectric interface, and have been attracting significant research interests given the recent advances in nanofabrication [10–14]. This has led to exciting advances in optical metamaterials, which have physical properties that cannot be found in macro-scale materials. Near-field nanolithography using colloidal nanospheres is an ideal fabrication technique for planar metamaterials [167, 182–187], where the devices are typically periodic with a uniform (as opposed to meta-surfaces [13, 14]) but complex unit-cell geometry. One example is shown in figure 14(a), where a hexagonal array of aligned Au ellipses are depicted [167]. These structures are patterned using photonic nanojet generated by illuminating an extended light source on a $1 \mu\text{m}$ diameter array of spheres and

then coated with Au. These anisotropic nanostructures are polarization sensitive, and can be used as a platform for surface enhanced infrared absorption in biosensing. The alignment of the structure results in preferential absorption along the major axis due to localized surface plasmon resonance. The peak absorption wavelength can be tuned by controlling the length and period of the major axis during exposure, as illustrated in the measured Fourier-transform infrared spectroscopy (FTIR) spectra shown in figure 14(a2). The absorption versus polarization alignment angle to the major axis is also plotted for Au nanoellipse array with $1.5 \mu\text{m}$ period and $1.15 \mu\text{m}$ major axis length, as shown in figure 14(a3). Here it can be observed that a significant absorption enhancement can be achieved for light that is within 15° of alignment.

Another example of a plasmonic nanostructure fabricated using photonic nanojet patterning is shown in figure 14(b), where a metal–insulator–metal (MIM) nanodisk array is used to study plasmon hybridization modes [182]. In this work, an

array of 500 nm diameter spheres were illuminated to pattern an array of holes in photoresist. Thin layers of Ag and SiO₂ with 15 nm thickness were then deposited to construct the MIM nanodisk structure using a lift-off process, as shown in figure 14(b1). Distinct from the typically dipole resonant mode observed for a single metal disk, the measured extinction spectra illustrate energy levels were two distinct hybridization modes, as shown in figure 14(b2). Here the lower energy mode exhibits anti-phase charge distribution that corresponds to the dark plasmon mode, which differs from the resonant mode at higher energy. The use of photonic nanojet for patterning can enable the large-scale manufacturing of such MIM plasmonic structures.

Other plasmonic devices include split-ring resonators (SRR), an important element in the construction of metamaterials and metasurfaces, as illustrated in figure 14(c) [186]. Here the structures were patterned using photonic nanojets created by off-axis illuminations of 3 μm diameter microspheres with 30° incident angle. The samples were continuously rotated by 345° to pattern the split-ring geometry. A 100 nm thick aluminum film is then deposited to construct the IR plasmonic device using a lift-off process. The FTIR spectra of the SRR device is shown in figure 14(c3), which has distinct reflectance response depending on the alignment of the electric field. When illuminated with IR radiation with polarization along the gap, the electric field is concentrated near both tips to generate a dipole response. The field distribution contours for the resonant modes for λ = 4.8 and 7.8 μm are shown in the inset diagrams. These results demonstrate that nanolithography using colloidal particles is a versatile, low-cost method to fabricate a wide range of plasmonic nanostructures.

5.2. Light-extraction nanostructures

Solid-state lighting such as light emitting diode (LED) and organic LED are promising approaches for energy-efficient lighting. However, one significant challenge that limits their efficiency is the trapping of light in the high-index active material medium. The light-extraction efficiency can be greatly enhanced using photonic nanostructures, as demonstrated in the recent literature [27–31]. However, most of these techniques require the use of expensive lithographic techniques, which can increase the production cost. In addition to the processing cost, it is also important for the efficient light-extracting nanostructures to be well-ordered and can be readily designed to have different geometries.

Near-field lithography using nanosphere array is an ideal approach for fabrication of light-extraction nanostructures that are highly efficient and low cost [188–190]. Examples of recent work in this area are shown in figure 15(a), which are the top-view SEM images of nanostructures on InGaN/GaN LEDs [188]. Fabricated using the Talbot effect with different spacer layer thickness, the 2D structure geometry includes hexagonal array of (i) holes, (ii) rods, (iii) rings, and (iv) anti-ring. In this experiment, an array of 1.2 μm diameter PS spheres were used to make a metal hole mask, which was then illuminated with 365 nm wavelength laser to pattern

photoresist separated by a transparent spacer layer. The photoluminescent (PL) measurements of the samples are shown in figure 15(a1), where the emissions are all centered around 460 nm. The normalized PL ($PL_{\text{rel}}/A_{\text{eff}}$) and the absolute light-extraction efficiency (LEE_{abs}) are also plotted for the reference planar and the nanostructured surfaces, which demonstrated the highest enhancement for the array of nanorods and nanorings.

Light-extraction nanostructures can also be fabricated in the photonic nanojet regimes using an array of larger nanospheres [189]. This technique is ideal for structures that require angular symmetry in the unit cell, which can be accomplished using multiple off-axis exposures. Examples are illustrated in figure 15(b), where the fabricated structures on GaN-based LEDs consist of hexagonal array of (b1) single, (b2) doublet, (b3) triplet, and (b4) quadruplet of holes. In these experiments, an array of 1.2 μm diameter PS spheres are illuminated with 365 nm wavelength light using multiple off-axis exposures. The electrical characterization of the device is shown in figure 15(b5), where the output light power and external quantum efficiencies for the different devices are plotted versus different device current. For injection current of 350 mA, the enhancement of output power when compared with LED with planar surface are 14.8%, 36.0%, 53.7%, and 44.9% for the single, doublet, triplet, and quadruplet structures, respectively. Here it can be observed that the light-extraction structures with higher-order unit-cell symmetry result in higher efficiency, with the maximum occurring for the triplet structures. The normalized far-field emission pattern for LEDs with planar and light-extraction structures are shown in figure 15(b6), which shows that the planar LED has a broader divergent angle. This is due to trapped light within the high-index substrate, which then escapes through multiple scattering events at oblique angles. It can be observed that the triplet structures have the lowest divergent angle, which indicates that light is most effectively diverted to the light escape cone.

5.3. Photonic crystals

Nanostructures that are periodic in three-dimensions, known as 3D PhCs, can have high narrowband reflectance efficiency, or perfect reflectance for lattice geometry with complete energy bandgap [1–4]. PhC can find applications in photonic circuits [107], optical sensors [5], and iridescent display [6, 7]. Consisting of complex 3D geometry, these typically require expensive fabrication methods using layer-by-layer processes or multiple beam interference lithography [2–5]. The Talbot intensity distribution generated by normal illumination of an array of nanospheres is also an effective method to fabricate 3D PhCs.

Fabrication of 3D PhC was demonstrated by Jeong *et al* [174] using UV illumination of PDMS mask embedded with PS nanospheres, as illustrated in figure 16. Here PhC with slightly different axial period z_r can be obtained by increasing the exposure dose, as shown in figures 16(a)–(c). This can result in a red shift in the reflected wavelength peak of the PhC, as illustrated in the measured reflectance spectra of the

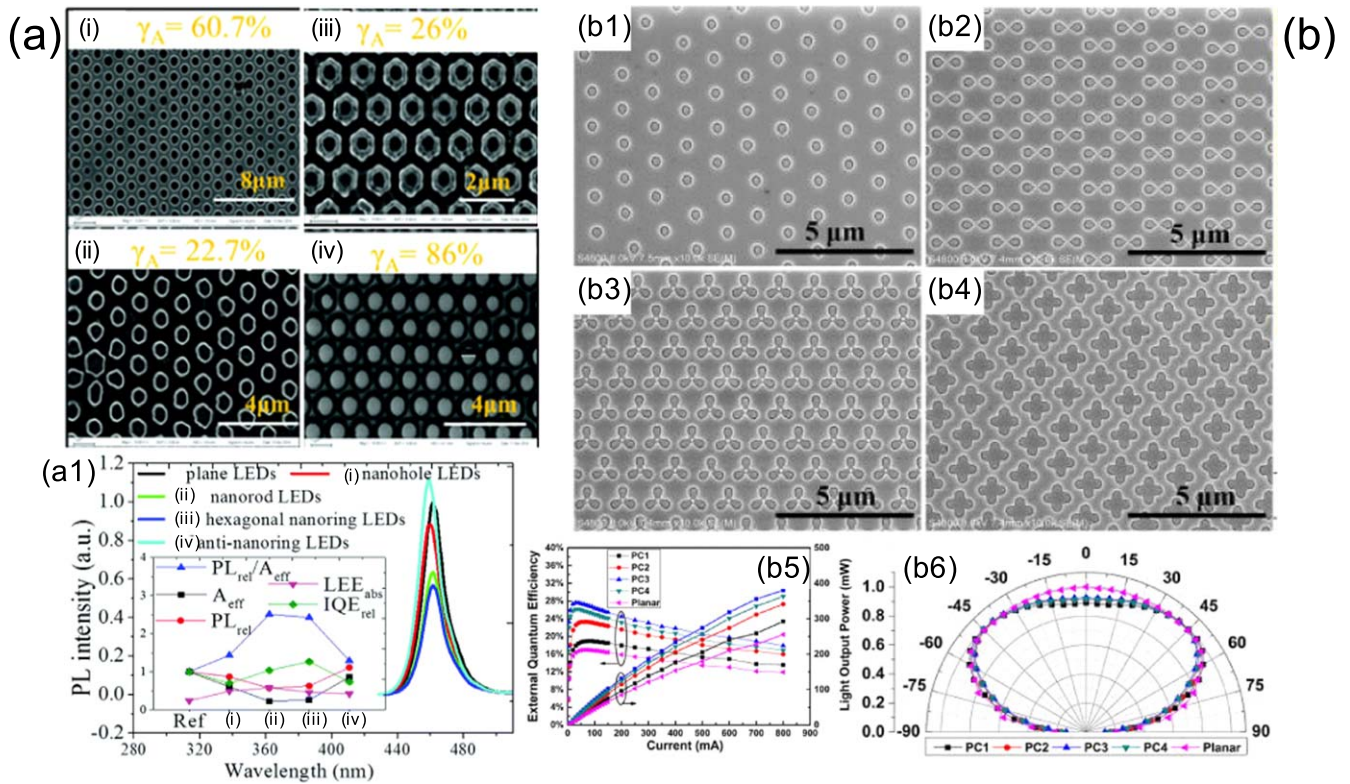


Figure 15. Fabrication of light-extraction nanostructures using normal illumination of nanosphere array. (a) Patterned InGaN/GaN LEDs with an array of (i) holes, (ii) rods, (iii) rings, and (iv) anti-ring structures using the Talbot effect. The effective area ratio (γ_A) is listed for each nanostructure. (a1) PL intensity of planar and nanostructured LEDs. The effective area (A_{eff}), relative PL intensity (PL_{rel}), PL intensity per area ($PL_{\text{rel}}/A_{\text{eff}}$), and absolute LEE (LEE_{abs}) are plotted in the inset diagram. Reproduced with permission [188] with permission of The Royal Society of chemistry (RSC) on behalf of the European Society for Photobiology, the European Photochemistry Association and the RSC. (b) Using multiple off-axis exposures, arrays of (b1) single hole, (b2) doublet, (b3) triplet, and (b4) quadruplet nanostructures can be patterned. (b5) Measured external quantum efficiencies and light output powers as functions of injection current for the all LEDs. (c) Normalized far-field emission patterns of LEDs with planar and nanostructured LEDs at an injection current of 350 mA. (b) and (c) reproduced with permission [189], with the permission of AIP Publishing.

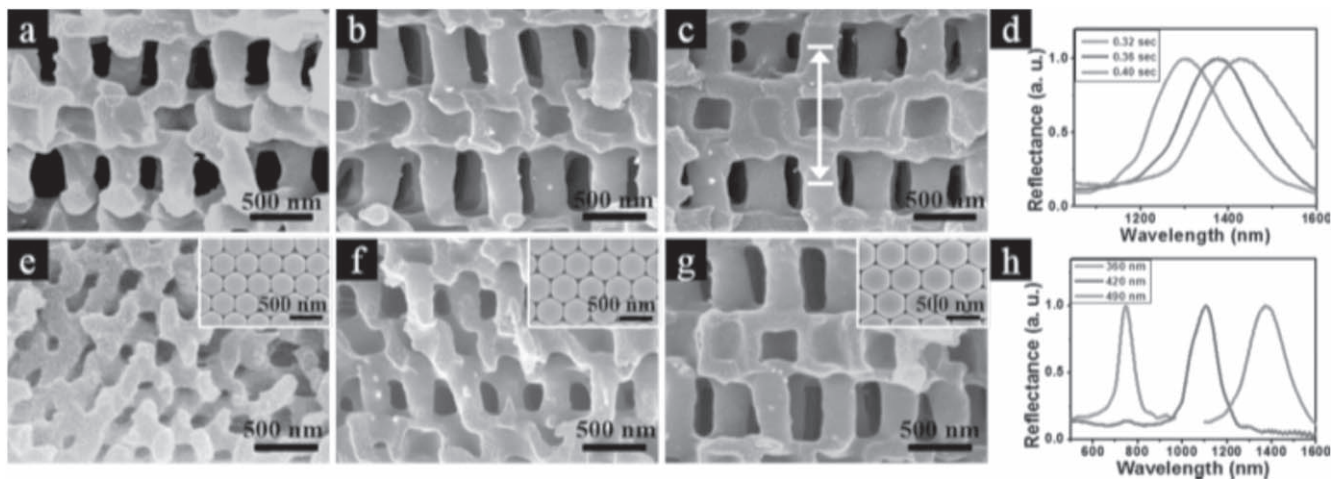


Figure 16. Using the Talbot effect, 3D photonic crystals can be patterned using normal illumination of nanosphere array. (a)–(c) Cross-section SEM images of 3D periodic nanostructures fabricated using 490 nm PS spheres with increasing exposure dose (exposure time of 0.32, 0.36, and 0.4 s) and (d) their corresponding reflectance spectra. (e)–(g) Cross-section SEM images of 3D periodic nanostructures fabricated using 360, 420, and 490 nm spheres and (h) their corresponding reflectance spectra. Reproduced with permission [174] John Wiley & Sons. © 2013 WILEY-VCH Verlag GmbH & Co. KGaA, Weinheim.

samples in figure 16(d). This can be attributed to higher crosslinking density, resulting in more rigid structures with less out-of-plane sagging. The structure can reflect $\sim 50\%$ of the light at the peak, illustrating strong PhC effect but an incomplete energy bandgap. Structures can also be patterned using different sphere diameters from 360, 420, to 490 nm, resulting in structures with increasing z_r , as shown in figures 16(e)–(g). The reflectance spectra for these samples are shown in figure 16(h), which shows a blue shift for the smaller lattice period from 1350 to 750 nm, as expected. It is also interesting to note that the PhC with smaller period also has a narrower reflectance spectrum, which is desirable for many applications.

Nanolithography using colloidal nanosphere is especially well suited for patterning PhC since the Talbot effect can lead to 3D structures using a single exposure, greatly reducing patterning time. In addition, the unit-cell geometry can be readily designed by the γ parameter, allowing PhC with different lattices to be fabricated. It is also possible to independently design the lateral and axial periods, since the former depends solely on the sphere diameter while the later can be tuned by the exposure wavelength. The ability to use physical templates to direct the colloidal assembly can also lead to photonic circuits with embedded PhC, as discussed in section 4.3. However, there are some drawbacks that must be considered. Since the wave vectors of the propagating modes in the photoresists are linked to the sphere array, they cannot be arbitrarily prescribed. This is in contrast to multiple beam interference lithography, in which all 14 Bravais lattices can be patterned [75]. It is also difficult to obtain structures with exactly the same lateral and axial lattice periods, which requires the γ parameter to approach 1. This limits the lattice structures that can be produced, which makes generating PhCs with complete energy bandgap difficult.

5.4. Multifunctional nanoarchitected materials

Mechanical properties of periodic 3D nanostructures have also attracted significant research attention. These are sometimes known as nanoarchitected materials or mechanical metamaterials [32–37], where they can exhibit unique physical properties that do not exist in nature. For example, recent work have demonstrated micro/nanolattices with negative Poisson's ratio [32], ultralow density [35, 36], and large strain recovery [37]. This research area is strongly dependent on the advancement of nanofabrication techniques, which need to be versatile, controllable, and scalable with high resolution. Most existing work in this field is done with two-photon lithography, which can pattern arbitrary 3D geometry for rapid prototyping but have low throughput. It is also highly desirable that these materials can exhibit multiple functionalities in different physical domains. For example, by creating nanolattices with period smaller than the wavelength of visible light, optical scattering can be minimized to render the material non-observable.

The 3D nanolithography using the Talbot effect is well suited to fabricate such multifunctional nanoarchitected

materials. It can be combined with atomic layer deposition (ALD) to create a new class of lightweight nanolattice material, as shown in figure 17(a) [191]. Here the 3D periodic nanostructures in photoresist are designed and patterned by illuminating a nanosphere array. Thin layers of materials can be deposited on the polymeric templates using ALD, which can be controlled with atomic precision. The polymeric templates can then be thermally decomposed or plasma etched to yield highly porous nanolattice materials. We have demonstrated a wide range of materials, such as Al_2O_3 , ZnO, TiO_2 , W, and Pt. Figure 17(b) depicts Al_2O_3 nanolattice material with 6.0 nm ALD coating thickness. The combination of 3D nanolithography and ALD enables the versatile control of lattice architecture and material composition, which in turn enables the design of the physical properties.

The nanolattice materials possess both superior optical and mechanical properties [191–193]. Demonstrated using spectroscopic ellipsometry as shown in figure 17(c), the nanolattice film can have refractive index as low as 1.025 [191]. Index up to 1.3 can also be fabricated by controlling the ALD film thickness and material composition, filling the index gap where no naturally occurring solids exist [194]. The periodic architecture and small period of this material can also reduce light scattering, leading to high optical clarity. The sample is placed next to a bare glass in the inset image, and no additional scattering can be visually observed. Such low-index films are especially useful in nanophotonics, where index contrast is desirable to enhance device performance [194–197]. The nanolattice film can be integrated into multilayer films to enhance total internal reflection [193], which can potentially improve light trapping in integrated photonic devices. This work demonstrates the feasibility of using nanolattice materials in multilayer photonic devices while maintaining the low-index behavior.

The nanolattice materials also exhibit superior mechanical property scaling at low density when compared with random porous structures [192]. Using nanoindentation with cyclic loading, the mechanical properties were characterized for Al_2O_3 and ZnO nanolattice films, as shown in figure 17(d). It was found that the tubular architectures give rise to favorable modulus-density scaling (power of ~ 1.1). The scaling outperforms or is comparable to previous reports where micro/nanolattices with micrometer lattice periods were studied [35–37]. The film also exhibits enhanced energy dissipation and high hardness at low density. At 95.6% porosity, the nanolattice film has demonstrated modulus of 1.19 GPa and specific energy dissipation of 325.5 kJ kg^{-1} , among the highest reported to date. The deformation mechanism of the film is dominated by buckling of the tubular elements, which shows a remarkable ability to fully recover for shell thickness less than 10 nm. This can be attributed to a transition between brittle fracture and ductile behaviors below the critical length scale. Such multifunctional nanolattice film can be used as a robust, air-like insulating layer for integrated photonics, optoelectronics, and microfluidic chips.

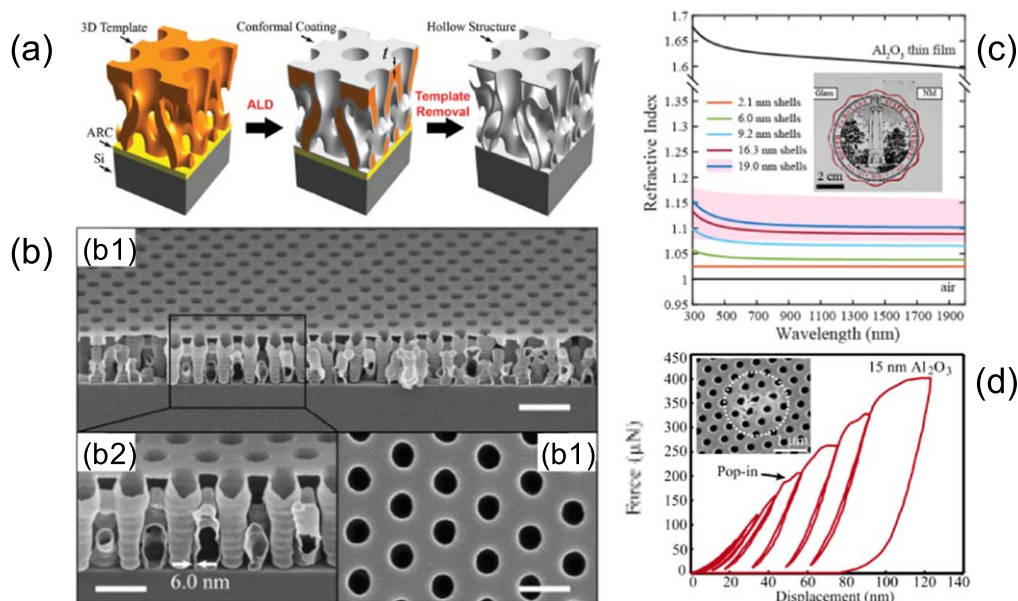


Figure 17. Fabrication of low-density nanolattice film using normal illumination of nanosphere array. (a) After patterning of 3D structures, conformal thin films can be deposited using ALD. (b) SEM images of the nanolattice materials with 6 nm thick Al_2O_3 shells. (c) Measured broadband refractive indices for nanolattice films, which can approach 1.025 for the thinnest sample. Reproduced with permission [191]. John Wiley & Sons. © 2015 WILEY-VCH Verlag GmbH & Co. KGaA, Weinheim. (d) Force–displacement curve of 15 nm thick Al_2O_3 nanolattice film measured using nanoindentation. Reprinted by permission from Macmillan Publishers Ltd: Scientific Reports [192], Copyright (2017).

5.5. Other potential applications

Beyond the demonstrated applications described in the previous section, near-field nanolithography using colloidal particles can also have an impact in other areas. One direction is 3D functional nanostructures, which are generally achieved by coating or infiltrating functional materials within a 3D nanostructured template. The intrinsic properties of the coated materials can be combined with the 3D structure to enable unique functionalities. Here a few potential applications are provided to serve as a guide for future development of the nanolithography techniques described in this review.

One potential direction is stretchable conductors with electrical and mechanical properties that can be independently designed. Porous polymer material with 3D architectures can be embedded with conductive materials to have superior sensor performance in terms of stretchability, cyclability, and sensitivity [198]. Here the 3D template was fabricated by phase lithography and replicated in PDMS, which is then infiltrated with carbon nanotubes to enable strain sensing. Polymer template can also be coated with ALD to enable nano-accordion structures that can be simultaneously stretchable, transparent, and conductive [199]. In photonics area, 3D ZnO hollow shell structures have been demonstrated using prism interference lithography and ALD [200]. This work demonstrates a tunable photonic bandgap that can be achieved using different ZnO coating thicknesses. Tuning of the photonic bandgap has also been demonstrated by coating tungsten or hafnium diboride in 3D colloidal assemblies to achieve inverse-opal structures [201]. In energy areas, ZnO nano-shell structures have shown anomalous thermoelectricity behavior, a significant improvement in figure of merit

over bulk ZnO [202]. Electroplated nickel replicated from 3D opal templates have also shown ultrafast charge cycle as battery electrodes [43]. The 3D lithography methods in the above examples are based on free-space interference of light, which can also be achieved using the techniques described in this review. Therefore, it is logical to use colloidal assembly-based near-field nanolithography to produce large-area 3D functional nanostructures cost-effectively without complex hardware and costly templates.

6. Conclusion and outlook

This review summarizes the recent developments in 3D near-field nanolithography using colloidal nanospheres. The emphasis is on the optical interactions that can be harnessed with the inclusion of colloidal elements in lithography systems. For a single nanosphere, Mie scattering can result in a highly focused central beam known as a photonic nanojet for subwavelength patterning. Angular scattering from smaller spheres can also generate unique 3D intensity distributions. The use of off-axis and multiple exposures can also lead to precise control over the unit-cell geometry and novel hollow 3D nanostructures with complex symmetries. For self-assembled nanospheres, two regimes can be identified. For large spheres the focusing effect dominates, generating an array of photonic nanojets that can be used for parallel direct-write patterning. For smaller spheres, near-field diffraction dominates, leading to the creation of 3D periodic intensity distribution as known as the Talbot effect. This allows the direct printing of periodic 3D nanostructures using a single normal exposure. Note that for all of these techniques, the

intensity pattern can be precisely designed by controlling the relative sphere size and illuminating wavelength. This approach employs widely available colloidal particles and does not require extensive hardware, greatly reducing the process cost of 3D nanolithography. This can be implemented in a table-top system, which can be readily accessible for small businesses and university laboratory. On the other hand, this process is also highly scalable and can be potentially implemented in a roll-to-roll manufacturing production line.

There are a number of unsolved challenges associated with this technique, the most critical being the assembly yield. For existing techniques, it is still difficult to obtain defect-free assembly across whole wafers, and most assemblies are polycrystalline with vacancies, grain boundaries, and dislocations. Such defects can degrade the exposure contrast, leading to structural collapse in the photoresist. One viable option to mitigate defect is to use microscale assembly templates, which can be patterned using standard microlithography approaches. There are also some limitations to the geometries that can be patterned, since the image formation mechanisms must obey the physics of scattering and diffraction. More efforts in computational lithography can potentially solve the inverse problem and lead to more patterns. Beyond exploring the lithography capabilities, post-processing can also broaden the impact of this technique. One approach is the deposition of other functional materials within the patterned 2D and 3D nanostructures, which can further expand applications in nanophotonics, optoelectronic devices, energy systems, and multifunctional nanostructured materials.

Acknowledgments

This work was performed at the NCSU Nanofabrication Facility (NNF) and the Analytical Instrumentation Facility (AIF), members of the North Carolina Research Triangle Nanotechnology Network (RTNN), which is supported by the National Science Foundation as part of the National Nanotechnology Coordinated Infrastructure (NNCI). This work was supported by the National Science Foundation (NSF) grant CMMI#1552424.

ORCID iDs

Chih-Hao Chang  <https://orcid.org/0000-0003-4268-4108>

References

- [1] Yablonovitch E 1987 Inhibited spontaneous emission in solid-state physics and electronics *Phys. Rev. Lett.* **58** 2059–62
- [2] Lin S Y, Fleming J G, Hetherington D L, Smith B K, Biswas R, Ho K M, Sigalas M M, Zubrzycki W, Kurtz S R and Bur J 1998 A three-dimensional photonic crystal operating at infrared wavelengths *Nature* **394** 251–3
- [3] Campbell M, Sharp D N, Harrison M T, Denning R G and Turberfield A J 2000 Fabrication of photonic crystals for the visible spectrum by holographic lithography *Nature* **404** 53–6
- [4] Qi M *et al* 2004 A three-dimensional optical photonic crystal with designed point defects *Nature* **429** 538–42
- [5] von Freymann G, Ledermann A, Thiel M, Staude I, Essig S, Busch K and Wegener M 2010 Three-dimensional nanostructures for photonics *Adv. Funct. Mater.* **20** 1038–52
- [6] Arsenault A C, Puzzo D P, Manners I and Ozin G A 2007 Photonic-crystal full-colour displays *Nat. Photon.* **1** 468–72
- [7] Aguirre C I, Reguera E and Stein A 2010 Tunable colors in opals and inverse opal photonic crystals *Adv. Funct. Mater.* **20** 2565–78
- [8] Valentine J, Zhang S, Zentgraf T, Ulin-Avila E, Genov D A, Bartal G and Zhang X 2008 Three-dimensional optical metamaterial with a negative refractive index *Nature* **455** 376–9
- [9] Ergin T, Stenger N, Brenner P, Pendry J B and Wegener M 2010 Three-dimensional invisibility cloak at optical wavelengths *Science* **328** 337–9
- [10] Boltasseva A and Atwater H A 2011 Low-loss plasmonic metamaterials *Science* **331** 290–1
- [11] Duan H, Fernández-Domínguez A I, Bosman M, Maier S A and Yang J K W 2012 Nanoplasmonics: classical down to the nanometer scale *Nano Lett.* **12** 1683–9
- [12] Kumar K, Duan H, Hegde R S, Koh S C W, Wei J N and Yang J K W 2012 Printing colour at the optical diffraction limit *Nat. Nanotechnol.* **7** 557–61
- [13] Yu N and Capasso F 2014 Flat optics with designer metasurfaces *Nat. Mater.* **13** 139–50
- [14] Kildishev A V, Boltasseva A and Shalaev V M 2013 Planar photonics with metasurfaces *Science* **339** 1232009
- [15] Shen B, Wang P, Polson R and Menon R 2015 An integrated-nanophotonics polarization beamsplitter with $2.4 \times 2.4 \mu\text{m}^2$ footprint *Nat. Photon.* **9** 378–82
- [16] Vukusic P and Sambles J R 2003 Photonic structures in biology *Nature* **424** 852–5
- [17] Parker A R and Townley H E 2007 Biomimetics of photonic nanostructures *Nat. Nanotechnol.* **2** 347–53
- [18] Kanamori Y, Sasaki M and Hane K 1999 Broadband antireflection gratings fabricated upon silicon substrates *Opt. Lett.* **24** 1422–4
- [19] Lalanne P and Morris G M 1997 Antireflection behavior of silicon subwavelength periodic structures for visible light *Nanotechnology* **8** 53–6
- [20] Min W-L, Jiang B and Jiang P 2008 Bioinspired self-cleaning antireflection coatings *Adv. Mater.* **20** 3914–8
- [21] Park K-C, Choi H J, Chang C-H, Cohen R E, McKinley G H and Barbastathis G 2012 Nanotextured silica surfaces with robust superhydrophobicity and omnidirectional broadband supertransmissivity *ACS Nano* **6** 3789–99
- [22] Yang Q, Zhang X A, Bagal A, Guo W and Chang C-H 2013 Antireflection effects at nanostructured material interfaces and the suppression of thin-film interference *Nanotechnology* **24** 235202
- [23] Fan Z *et al* 2009 Three-dimensional nanopillar-array photovoltaics on low-cost and flexible substrates *Nat. Mater.* **8** 648–53
- [24] Jung J-Y, Guo Z, Jee S-W, Um H-D, Park K-T and Lee J-H 2010 A strong antireflective solar cell prepared by tapering silicon nanowires *Opt. Express* **18** A286–92
- [25] Zhu J, Hsu C-M, Yu Z, Fan S and Cui Y 2010 Nanodome solar cells with efficient light management and self-cleaning *Nano Lett.* **10** 1979–84
- [26] Ko D-H, Tumbleston J R, Gadisa A, Aryal M, Liu Y, Lopez R and Samulski E T 2011 Light-trapping nano-

- structures in organic photovoltaic cells *J. Mater. Chem.* **21** 16293–303
- [27] Fujii T, Gao Y, Sharma R, Hu E L, DenBaars S P and Nakamura S 2004 Increase in the extraction efficiency of GaN-based light-emitting diodes via surface roughening *Appl. Phys. Lett.* **84** 855–7
- [28] So F, Kido J and Burrows P 2008 Organic light-emitting devices for solid-state lighting *MRS Bull.* **33** 663–9
- [29] Frischeisen J, Niu Q, Abdellah A, Kinzel J B, Gehlhaar R, Scarpa G, Adachi C, Lugli P and Brütting W 2011 Light extraction from surface plasmons and waveguide modes in an organic light-emitting layer by nanoimprinted gratings *Opt. Express* **19** A7–19
- [30] Youn W, Lee J, Xu M, Singh R and So F 2015 Corrugated sapphire substrates for organic light-emitting diode light extraction *ACS Appl. Mater. Interfaces* **7** 8974–8
- [31] Koo W H, Youn W, Zhu P, Li X-H, Tansu N and So F 2012 Light extraction of organic light emitting diodes by defective hexagonal-close-packed array *Adv. Funct. Mater.* **22** 3454–9
- [32] Greaves G N, Greer A L, Lakes R S and Rouxel T 2011 Poisson's ratio and modern materials *Nat. Mater.* **10** 823–37
- [33] Lee J-H, Wang L, Kooi S, Boyce M C and Thomas E L 2010 Enhanced energy dissipation in periodic epoxy nanoframes *Nano Lett.* **10** 2592–7
- [34] Lee J-H, Singer J P and Thomas E L 2012 Micro-/nanostructured mechanical metamaterials *Adv. Mater.* **24** 4782–810
- [35] Schaedler T A, Jacobsen A J, Torrents A, Sorensen A E, Lian J, Greer J R, Valdevit L and Carter W B 2011 Ultralight metallic microlattices *Science* **334** 962–5
- [36] Zheng X *et al* 2014 Ultralight, ultrastiff mechanical metamaterials *Science* **344** 1373–7
- [37] Meza L R, Das S and Greer J R 2014 Strong, lightweight, and recoverable three-dimensional ceramic nanolattices *Science* **345** 1322–6
- [38] Lafuma A and Quéré D 2003 Superhydrophobic states *Nat. Mater.* **2** 457–60
- [39] Lau K K S, Bico J, Teo K B K, Chhowalla M, Amaratunga G A J, Milne W I, McKinley G H and Gleason K K 2003 Superhydrophobic carbon nanotube forests *Nano Lett.* **3** 1701–5
- [40] Parker A R and Lawrence C R 2001 Water capture by a desert beetle *Nature* **414** 33–4
- [41] Zhai L, Berg M C, Cebeci F Ç, Kim Y, Milwid J M, Rubner M F and Cohen R E 2006 Patterned superhydrophobic surfaces: toward a synthetic mimic of the namib desert beetle *Nano Lett.* **6** 1213–7
- [42] Koch K and Barthlott W 2009 Superhydrophobic and superhydrophilic plant surfaces: an inspiration for biomimetic materials *Phil. Trans. R. Soc. A* **367** 1487–509
- [43] Zhang H, Yu X and Braun P V 2011 Three-dimensional bicontinuous ultrafast-charge and -discharge bulk battery electrodes *Nat. Nanotechnol.* **6** 277–81
- [44] Pikul J H, Gang Zhang H, Cho J, Braun P V and King W P 2013 High-power lithium ion microbatteries from interdigitated three-dimensional bicontinuous nanoporous electrodes *Nat. Commun.* **4** 1732
- [45] Yavuz M S *et al* 2009 Gold nanocages covered by smart polymers for controlled release with near-infrared light *Nat. Mater.* **8** 935–9
- [46] Moon G D, Choi S-W, Cai X, Li W, Cho E C, Jeong U, Wang L V and Xia Y 2011 A new theranostic system based on gold nanocages and phase-change materials with unique features for photoacoustic imaging and controlled release *J. Am. Chem. Soc.* **133** 4762–5
- [47] Prausnitz M R and Langer R 2008 Transdermal drug delivery *Nat. Biotechnol.* **26** 1261–8
- [48] Peer E, Artzy-Schnirman A, Gepstein L and Sivan U 2012 Hollow nanoneedle array and its utilization for repeated administration of biomolecules to the same cells *ACS Nano* **6** 4940–6
- [49] Yan L, Yang Y, Zhang W and Chen X 2014 Advanced materials and nanotechnology for drug delivery *Adv. Mater.* **26** 5533–40
- [50] Liddle J A and Gallatin G M 2016 Nanomanufacturing: a perspective *ACS Nano* **10** 2995–3014
- [51] Madou M J 2011 *Fundamentals of Microfabrication and Nanotechnology* (Boca Raton, FL: CRC Press)
- [52] Yamazaki K and Yamaguchi H 2008 Three-dimensional alignment with 10 nm order accuracy in electron-beam lithography on rotated sample for three-dimensional nanofabrication *J. Vac. Sci. Technol. B* **26** 2529–33
- [53] Chang T H P, Mankos M, Lee K Y and Muray L P 2001 Multiple electron-beam lithography *Microelectron. Eng.* **57–58** 117–35
- [54] Jeon J, Floresca H C and Kim M J 2000 Fabrication of complex three-dimensional nanostructures using focused ion beam and nanomanipulation *J. Vac. Sci. Technol. B* **28** 549–53
- [55] Winston D *et al* 2011 Neon ion beam lithography (NIBL) *Nano Lett.* **11** 4343–7
- [56] Winston D *et al* 2009 Scanning-helium-ion-beam lithography with hydrogen silsesquioxane resist *J. Vac. Sci. Technol. B* **27** 2702–6
- [57] Salaita K, Lee S W, Wang X, Huang L, Dellinger T M, Liu C and Mirkin C A 2005 Sub-100 nm, centimeter-scale, parallel dip-pen nanolithography *Small* **1** 940–5
- [58] Salaita K, Wang Y and Mirkin C A 2007 Applications of dip-pen nanolithography *Nat. Nanotechnol.* **2** 145–55
- [59] Szoszkiewicz R, Okada T, Jones S C, Li T-D, King W P, Marder S R and Riedo E 2007 High-speed, sub-15 nm feature size thermochemical nanolithography *Nano Lett.* **7** 1064–9
- [60] Brown K A, Eichelsdoerfer D J, Shim W, Rasin B, Radha B, Liao X, Schmucker A L, Liu G and Mirkin C A 2013 A cantilever-free approach to dot-matrix nanoprinting *Proc. Natl Acad. Soc.* **110** 12921–4
- [61] Huang Z, Li L, Zhang X A, Alsharif N, Wu X, Peng Z, Cheng X, Wang P, Brown K A and Wang Y 2018 Photoactuated pens for molecular printing *Adv. Mater.* **30** 1705303
- [62] Maruo S, Nakamura O and Kawata S 1997 Three-dimensional microfabrication with two-photon-absorbed photopolymerization *Opt. Lett.* **22** 132–4
- [63] Cumpston B H *et al* 1999 Two-photon polymerization initiators for three-dimensional optical data storage and microfabrication *Nature* **398** 51–4
- [64] Kawata S, Sun H-B, Tanaka T and Takada K 2001 Finer features for functional microdevices *Nature* **412** 697–8
- [65] Haske W, Chen V W, Hales J M, Dong W, Barlow S, Marder S R and Perry J W 2007 65 nm feature sizes using visible wavelength 3D multiphoton lithography *Opt. Express* **15** 3426–36
- [66] Chou S Y, Krauss P R and Renstrom P J 1995 Imprint of sub-25 nm vias and trenches in polymers *Appl. Phys. Lett.* **67** 3114
- [67] Colburn M *et al* 1999 Step and flash imprint lithography: a new approach to high-resolution patterning microlithography *Proc. SPIE* **3676** 379
- [68] Guo L J 2007 Nanoimprint lithography: methods and material requirements *Adv. Mater.* **19** 495–513
- [69] Ahn S H and Guo L J 2008 High-speed roll-to-roll nanoimprint lithography on flexible plastic substrates *Adv. Mater.* **20** 2044–9
- [70] Ahn S H and Guo L J 2009 Large-area roll-to-roll and roll-to-plate nanoimprint lithography: a step toward high-throughput application of continuous nanoimprinting *ACS Nano* **3** 2304–10

- [71] Sreenivasan S V 2017 Nanoimprint lithography steppers for volume fabrication of leading-edge semiconductor integrated circuits *Nanoeng.* **3** 17075
- [72] Shank C V and Schmidt R V 1973 Optical technique for producing 0.1- μ periodic surface structures *Appl. Phys. Lett.* **23** 154–5
- [73] Divliansky I, Mayer T S, Holliday K S and Crespi V H 2003 Fabrication of three-dimensional polymer photonic crystal structures using single diffraction element interference lithography *Appl. Phys. Lett.* **82** 1667–9
- [74] Smith H I 2001 Low cost nanolithography with nanoaccuracy *Physica E* **11** 104–9
- [75] Cai L Z, Yang X L and Wang Y R 2002 All fourteen Bravais lattices can be formed by interference of four noncoplanar beams *Opt. Lett.* **27** 900–2
- [76] Jang J-H, Ullal C K, Maldovan M, Gorishnyy T, Kooi S, Koh C and Thomas E L 2007 3D micro- and nanostructures via interference lithography *Adv. Funct. Mater.* **17** 3027–41
- [77] Chang C-H, Zhao Y, Heilmann R K and Schattenburg M L 2008 Fabrication of 50 nm period gratings with multilevel interference lithography *Opt. Lett.* **33** 1572–4
- [78] Bagal A and Chang C-H 2013 Fabrication of subwavelength periodic nanostructures using liquid immersion lloyd's mirror interference lithography *Opt. Lett.* **38** 2531–4
- [79] Wathuthanthri I, Liu Y, Du K, Xu W and Choi C-H 2013 Simple holographic patterning for high-aspect-ratio three-dimensional nanostructures with large coverage area *Adv. Funct. Mater.* **23** 608–18
- [80] Wu L, Zhong Y, Chan C T, Wong K S and Wang G P 2005 Fabrication of large area two- and three-dimensional polymer photonic crystals using single refracting prism holographic lithography *Appl. Phys. Lett.* **86** 241102
- [81] Jeon S, Park J-U, Cirelli R, Yang S, Heitzman C E, Braun P V, Kenis P J A and Rogers J A 2004 Fabricating complex three-dimensional nanostructures with high-resolution conformable phase masks *Proc. Natl Acad. Sci.* **101** 12428–33
- [82] Shir D, Nelson E C, Chen Y C, Brzezinski A, Liao H, Braun P V, Wiltzius P, Bogart K H A and Rogers J A 2009 Three dimensional silicon photonic crystals fabricated by two photon phase mask lithography *Appl. Phys. Lett.* **94** 011101
- [83] George M C, Nelson E C, Rogers J A and Braun P V 2009 Direct fabrication of 3D periodic inorganic microstructures using conformal phase masks *Angew. Chem., Int. Ed.* **48** 144–8
- [84] Isoyan A, Jiang F, Cheng Y C, Cerrina F, Wachulak P, Urbanski L, Rocca J, Menoni C and Marconi M 2009 Talbot lithography: self-imaging of complex structures *J. Vac. Sci. Technol. B* **27** 2931–7
- [85] Jang J-W, Zheng Z, Lee O-S, Shim W, Zheng G, Schatz G C and Mirkin C A 2010 Arrays of nanoscale lenses for subwavelength optical lithography *Nano Lett.* **10** 4399–404
- [86] Hyun J K, Park J, Kim E, Lauhon L J and Jeon S 2014 Rational control of diffraction and interference from conformal phase gratings: toward high-resolution 3D nanopatterning *Adv. Opt. Mater.* **2** 1213–20
- [87] Park M, Harrison C, Chaikin P M, Register R A and Adamson D H 1997 Block copolymer lithography: periodic arrays of ~ 1011 holes in 1 square centimeter *Science* **276** 1401–4
- [88] Kausch G and Magerale R 2002 Nanostructured thin films via self-assembly of block copolymers *Adv. Mater.* **14** 1579–83
- [89] Cheng J Y, Ross C A, Smith H I and Thomas E L 2006 Templated self-assembly of block copolymers: top-down helps bottom-up *Adv. Mater.* **18** 2505–21
- [90] Ruiz R, Kang H, Detcheverry F A, Dobisz E, Kercher D S, Albrecht T R, de Pablo J J and Nealey P F 2008 Density multiplication and improved lithography by directed block copolymer assembly *Science* **321** 936–9
- [91] Bita I, Yang J K W, Jung Y S, Ross C A, Thomas E L and Berggren K K 2008 Graphoepitaxy of self-assembled block copolymers on two-dimensional periodic patterned templates *Science* **321** 939–43
- [92] Park S, Lee D H, Xu J, Kim B, Hong S W, Jeong U, Xu T and Russell T P 2009 Macroscopic 10-terabit-per-square-inch arrays from block copolymers with lateral order *Science* **323** 1030–3
- [93] Pinto Y Y, Le J D, Seeman N C, Musier-Forsyth K, Taton T A and Kiehl R A 2005 Sequence-encoded self-assembly of multiple-nanocomponent arrays by 2D DNA scaffolding *Nano Lett.* **5** 2399–402
- [94] Rothmund P W K 2006 Folding DNA to create nanoscale shapes and patterns *Nature* **440** 297–302
- [95] Maune H T, Han S, Barish R D, Bockrath M, Iii W A G, Rothmund P W K and Winfree E 2009 Self-assembly of carbon nanotubes into two-dimensional geometries using DNA origami templates *Nat. Nanotechnol.* **5** 61–6
- [96] Denkov N D *et al* 1993 Two-dimensional crystallization *Nature* **361** 26
- [97] Velev O D, Jede T A, Lobo R F and Lenhoff A M 1997 Porous silica via colloidal crystallization *Nature* **389** 447–8
- [98] Velev O D and Kaler E W 2000 Structured porous materials via colloidal crystal templating: from inorganic oxides to metals *Adv. Mater.* **12** 531–4
- [99] Gates B, Qin D and Xia Y 1999 Assembly of nanoparticles into opaline structures over large areas *Adv. Mater.* **11** 466–9
- [100] Xia Y, Gates B, Yin Y and Lu Y 2000 Monodispersed colloidal spheres: old materials with new applications *Adv. Mater.* **12** 693–713
- [101] Prevo B G and Velev O D 2004 Controlled, rapid deposition of structured coatings from micro- and nanoparticle suspensions *Langmuir* **20** 2099–107
- [102] Velev O and Gupta S 2009 Materials fabricated by micro- and nanoparticle assembly—the challenging path from science to engineering *Adv. Mater.* **21** 1897–905
- [103] Jiang P and McFarland M J 2004 Large-scale fabrication of wafer-size colloidal crystals, macroporous polymers and nanocomposites by spin-coating *J. Am. Chem. Soc.* **126** 13778–86
- [104] Chen X, Lenhart S, Hirtz M, Lu N, Fuchs H and Chi L 2007 Langmuir–Blodgett patterning: a bottom-up way to build mesostructures over large areas *Acc. Chem. Res.* **40** 393–401
- [105] Li X and Gilchrist J F 2016 Large-area nanoparticle films by continuous automated Langmuir–Blodgett assembly and deposition *Langmuir* **32** 1220–6
- [106] Yin Y, Lu Y, Gates B and Xia Y 2001 Template-assisted self-assembly: a practical route to complex aggregates of monodispersed colloids with well-defined sizes, shapes, and structures *J. Am. Chem. Soc.* **123** 8718–29
- [107] Yang S M, Míguez H and Ozin G A 2002 Opal circuits of light—planarized microphotonic crystal chips *Adv. Funct. Mater.* **12** 425–31
- [108] Xia Y, Yin Y, Lu Y and McLellan J 2003 Template-assisted self-assembly of spherical colloids into complex and controllable structures *Adv. Funct. Mater.* **13** 907–18
- [109] Koh K, Hwang H, Park C, Lee J Y, Jeon T Y, Kim S-H, Kim J K and Jeong U 2016 Large-area accurate position registry of microparticles on flexible, stretchable substrates using elastomer templates *ACS Appl. Mater. Interfaces* **8** 28149–58
- [110] Deckman H W and Dunsmuir J H 1982 Natural lithography *Appl. Phys. Lett.* **41** 377–9

- [111] Hultheen J C and Duyne R P V 1995 Nanosphere lithography: a materials general fabrication process for periodic particle array surfaces *J. Vac. Sci. Technol. A* **13** 1553–8
- [112] Haynes C L and Van Duyne R P 2001 Nanosphere lithography: a versatile nanofabrication tool for studies of size-dependent nanoparticle optics *J. Phys. Chem. B* **105** 5599–611
- [113] Yang S-M, Jang S G, Choi D-G, Kim S and Yu H K 2006 Nanomachining by colloidal lithography *Small* **2** 458–75
- [114] Chang C-H, Dominguez-Caballero J A, Choi H J and Barbastathis G 2011 Nanostructured gradient-index antireflection diffractive optics *Opt. Lett.* **36** 2354–6
- [115] Vogel N, Retsch M, Fustin C-A, del Campo A and Jonas U 2015 Advances in colloidal assembly: the design of structure and hierarchy in two and three dimensions *Chem. Rev.* **115** 6265–311
- [116] Ye X and Qi L 2011 Two-dimensionally patterned nanostructures based on monolayer colloidal crystals: controllable fabrication, assembly, and applications *Nano Today* **6** 608–31
- [117] Liang X, Dong R and Ho J C 2019 Self-assembly of colloidal spheres toward fabrication of hierarchical and periodic nanostructures for technological applications *Adv. Mater. Technol.* **4** 1800541
- [118] Zhang Z, Geng C, Hao Z, Wei T and Yan Q 2016 Recent advancement on micro-/nano-spherical lens photolithography based on monolayer colloidal crystals *Adv. Colloid Interface Sci.* **228** 105–22
- [119] Wang Y, Zhang M, Lai Y and Chi L 2018 Advanced colloidal lithography: from patterning to applications *Nano Today* **22** 36–61
- [120] Wang Z, Ai B, Möhwald H and Zhang G 2018 Colloidal lithography meets plasmonic nanochemistry *Adv. Opt. Mater.* **6** 1800402
- [121] Xia Y, Xiong Y, Lim B and Skrabalak S E 2009 Shape-controlled synthesis of metal nanocrystals: simple chemistry meets complex physics? *Angew. Chem., Int. Ed.* **48** 60–103
- [122] Henzie J, Grünwald M, Widmer-Cooper A, Geissler P L and Yang P 2012 Self-assembly of uniform polyhedral silver nanocrystals into densest packings and exotic superlattices *Nat. Mater.* **11** 131–7
- [123] Chen Z, Taflove A and Backman V 2004 Photonic nanojet enhancement of backscattering of light by nanoparticles: a potential novel visible-light ultramicroscopy technique *Opt. Express* **12** 1214–20
- [124] Li X, Chen Z, Taflove A and Backman V 2005 Optical analysis of nanoparticles via enhanced backscattering facilitated by 3D photonic nanojets *Opt. Express* **13** 526–33
- [125] Lecler S, Takakura Y and Meyrueis P 2005 Properties of a three-dimensional photonic jet *Opt. Lett.* **30** 2641
- [126] Itagi A V and Challener W A 2005 Optics of photonic nanojets *J. Opt. Soc. Am. A* **22** 2847–58
- [127] Ferrand P, Wenger J, Devilez A, Pianta M, Stout B, Bonod N, Popov E and Rigneault H 2008 Direct imaging of photonic nanojets *Opt. Express* **16** 6930
- [128] Kim M-S, Scharf T, Mühlig S, Rockstuhl C and Herzig H P 2011 Engineering photonic nanojets *Opt. Express* **19** 10206–20
- [129] Luk'yanchuk B S, Paniagua-Domínguez R, Minin I, Minin O and Wang Z 2017 Refractive index less than two: photonic nanojets yesterday, today and tomorrow [invited] *Opt. Mater. Express* **7** 1820–47
- [130] Shen Y, Wang L V and Shen J-T 2014 Ultralong photonic nanojet formed by a two-layer dielectric microsphere *Opt. Lett.* **39** 4120–3
- [131] Liu C-Y 2012 Superenhanced photonic nanojet by core-shell microcylinders *Phys. Lett. A* **376** 1856–60
- [132] Yue L, Yan B, Monks J N, Wang Z, Tung N T, Lam V D, Minin O and Minin I 2017 Production of photonic nanojets by using pupil-masked 3D dielectric cuboid *J. Phys. D: Appl. Phys.* **50** 175102
- [133] Liu C-Y and Chang L-J 2014 Photonic nanojet modulation by elliptical microcylinders *Optik* **125** 4043–6
- [134] Liu C-Y 2014 Photonic nanojet shaping of dielectric non-spherical microparticles *Physica E* **64** 23–8
- [135] Yang S and Astratov V N 2008 Photonic nanojet-induced modes in chains of size-disordered microspheres with an attenuation of only 0.08dB per sphere *Appl. Phys. Lett.* **92** 261111
- [136] Kong S-C, Sahakian A, Taflove A and Backman V 2008 Photonic nanojet-enabled optical data storage *Opt. Express* **16** 13713–9
- [137] Wang Z, Guo W, Li L, Luk'yanchuk B, Khan A, Liu Z, Chen Z and Hong M 2011 Optical virtual imaging at 50 nm lateral resolution with a white-light nanoscope *Nat. Commun.* **2** 218
- [138] Yang H, Trouillon R, Huszka G and Gijis M A M 2016 Super-resolution imaging of a dielectric microsphere is governed by the waist of its photonic nanojet *Nano Lett.* **16** 4862–70
- [139] Neves A A R 2015 Photonic nanojets in optical tweezers *J. Quant. Spectrosc. Radiat. Transfer* **162** 122–32
- [140] Li Y, Xin H, Liu X, Zhang Y, Lei H and Li B 2016 Trapping and detection of nanoparticles and cells using a parallel photonic nanojet array *ACS Nano* **10** 5800–8
- [141] Li Y-C, Xin H-B, Lei H-X, Liu L-L, Li Y-Z, Zhang Y and Li B-J 2016 Manipulation and detection of single nanoparticles and biomolecules by a photonic nanojet *Light: Sci. Appl.* **5** e16176
- [142] Kovrov A, Novitsky A, Karabchevsky A and Shalin A S 2018 A photonic nanojet as tunable and polarization-sensitive optical tweezers *Ann. Phys.* **530** 1800129
- [143] Luk'yanchuk B, Zheng Y W and Lu Y F 2000 Laser cleaning of solid surface: optical resonance and near-field effects *Proc. SPIE* **4065** 576–87
- [144] Lu Y F, Zhang L, Song W D, Zheng Y W and Luk'yanchuk B S 2000 Laser writing of a subwavelength structure on silicon (100) surfaces with particle-enhanced optical irradiation *J. Exp. Theor. Phys. Lett.* **72** 457–9
- [145] Mosbacher M, Münzer H-J, Zimmermann J, Solis J, Boneberg J and Leiderer P 2001 Optical field enhancement effects in laser-assisted particle removal *Appl. Phys. A* **72** 41–4
- [146] Huang S M, Hong M H, Luk'yanchuk B S, Zheng Y W, Song W D, Lu Y F and Chong T C 2002 Pulsed laser-assisted surface structuring with optical near-field enhanced effects *J. Appl. Phys.* **92** 2495–500
- [147] Piglmayer K, Denk R and Bäuerle D 2002 Laser-induced surface patterning by means of microspheres *Appl. Phys. Lett.* **80** 4693–5
- [148] Leiderer P, Bartels C, König-Birk J, Mosbacher M and Boneberg J 2004 Imaging optical near-fields of nanostructures *Appl. Phys. Lett.* **85** 5370–2
- [149] McLeod E and Arnold C B 2008 Subwavelength direct-write nanopatterning using optically trapped microspheres *Nat. Nanotechnol.* **3** 413–7
- [150] Duocastella M, Tantussi F, Haddadpour A, Zaccaria R P, Jacassi A, Veronis G, Diaspro A and Angelis F D 2017 Combination of scanning probe technology with photonic nanojets *Sci. Rep.* **7** 3474
- [151] Jacassi A, Tantussi F, Dipalo M, Biagini C, Maccaferri N, Bozzola A and De Angelis F 2017 Scanning probe photonic nanojet lithography *ACS Appl. Mater. Interfaces* **9** 32386–93
- [152] Zhang X A, Elek J and Chang C-H 2013 Three-dimensional nanolithography using light scattering from colloidal particles *ACS Nano* **7** 6212–8

- [153] Kühler P, García de Abajo F J, Solis J, Mosbacher M, Leiderer P, Afonso C N and Siegel J 2009 Imprinting the optical near field of microstructures with nanometer resolution *Small* **5** 1825–9
- [154] Zhang X A, Dai B, Xu Z and Chang C-H 2015 Sculpting asymmetric, hollow-core, three-dimensional nanostructures using colloidal particles *Small* **11** 1285–92
- [155] Poteet A, Zhang X A, Nagai H and Chang C-H 2018 Twin photonic nanojets generated from coherent illumination of microscale sphere and cylinder *Nanotechnology* **29** 075204
- [156] Nagai H, Poteet A, Zhang X A and Chang C-H 2017 Three-dimensional colloidal interference lithography *Nanotechnology* **28** 125302
- [157] Winthrop J T and Worthington C R 1965 Theory of fresnel images: I. Plane periodic objects in monochromatic light* *J. Opt. Soc. Am.* **55** 373–81
- [158] Wen J, Zhang Y and Xiao M 2013 The Talbot effect: recent advances in classical optics, nonlinear optics, and quantum optics *Adv. Opt. Photon.* **5** 83–130
- [159] Wu W, Katsnelson A, Memis O G and Mohseni H 2007 A deep sub-wavelength process for the formation of highly uniform arrays of nanoholes and nanopillars *Nanotechnology* **18** 485302
- [160] Lu Y and Chen S C 2003 Nanopatterning of a silicon surface by near-field enhanced laser irradiation *Nanotechnol.* **14** 505–8
- [161] Guo W, Wang Z B, Li L, Whitehead D J, Luk'yanchuk B S and Liu Z 2007 Near-field laser parallel nanofabrication of arbitrary-shaped patterns *Appl. Phys. Lett.* **90** 243101
- [162] Liu X, Wang J, Li L, Gou J, Zheng J, Huang Z and Pan R 2018 Fabrication of hexagonal star-shaped and ring-shaped patterns arrays by Mie resonance sphere-lens-lithography *Appl. Surf. Sci.* **440** 378–85
- [163] Bonakdar A, Rezaei M, Brown R L, Fathipour V, Dexheimer E, Jang S J and Mohseni H 2015 Deep-UV microsphere projection lithography *Opt. Lett.* **40** 2537–40
- [164] Yeo J-B and Lee H-Y 2012 Realization of multi-paired photonic crystals by the multiple-exposure nanosphere lithography process *Scr. Mater.* **66** 311–4
- [165] Geng C, Yan Q, Du C, Dong P, Zhang L, Wei T, Hao Z, Wang X and Shen D 2014 Large-area and ordered sexfoil pore arrays by spherical-lens photolithography *ACS Photonics* **1** 754–60
- [166] David C, Kühler P, de Abajo F J G and Siegel J 2014 Near-field nanoimprinting using colloidal monolayers *Opt. Express* **22** 8226–33
- [167] Chang Y-C, Lu S-C, Chung H-C, Wang S-M, Tsai T-D and Guo T-F 2013 High-throughput nanofabrication of infra-red and chiral metamaterials using nanospherical-lens lithography *Sci. Rep.* **3** 3339
- [168] Chang C-H, Tian L, Hesse W R, Gao H, Choi H J, Kim J-G, Siddiqui M and Barbastathis G 2011 From two-dimensional colloidal self-assembly to three-dimensional nanolithography *Nano Lett.* **11** 2533–7
- [169] Min J-H, Zhang X A and Chang C-H 2016 Designing unit cell in three-dimensional periodic nanostructures using colloidal lithography *Opt. Express* **24** A276–84
- [170] Elek J E, Zhang X A, Dai B, Xu Z and Chang C-H 2015 Fabrication of three-dimensional hierarchical nanostructures using template-directed colloidal assembly *Nanoscale* **7** 4406–10
- [171] Yoon Jeon T, Chul Jeon H, Yang S-M and Kim S-H 2016 Hierarchical nanostructures created by interference of high-order diffraction beams *J. Mater. Chem. C* **4** 1088–95
- [172] Wu M-H, Paul K E and Whitesides G M 2002 Patterning flood illumination with microlens arrays *Appl. Opt.* **41** 2575–85
- [173] Wu M-H, Park C and Whitesides G M 2003 Generation of submicrometer structures by photolithography using arrays of spherical microlenses *J. Colloid Interface Sci.* **265** 304–9
- [174] Jeon T Y, Jeon H C, Lee S Y, Shim T S, Kwon J-D, Park S-G and Yang S-M 2014 3D hierarchical architectures prepared by single exposure through a highly durable colloidal phase mask *Adv. Mater.* **26** 1422–6
- [175] Fang M, Lin H, Cheung H-Y, Xiu F, Shen L, Yip S, Pun E Y-B, Wong C-Y and Ho J C 2014 Polymer-confined colloidal monolayer: a reusable soft photomask for rapid wafer-scale nanopatterning *ACS Appl. Mater. Interfaces* **6** 20837–41
- [176] Fang M, Lin H, Cheung H-Y, Yip S, Xiu F, Wong C-Y and Ho J C 2014 Optical nanoscale patterning through surface-textured polymer films *Adv. Opt. Mater.* **2** 855–60
- [177] Xue M, Cai X and Chen G 2015 Colloidal pen lithography *Small* **11** 548–52
- [178] Liu X, Li X, Li L, Chen W and Luo X 2015 Influence of sphere-surface distance and exposure dose on resolution of sphere-lens-array lithography *Opt. Express* **23** 30136–42
- [179] Geng C, Fan Y, Shi S, Yan Q, Wang L, Xu S, Zhang Y, Zhang Z-H and Bi W 2017 3D nanohole arrays generated by spherical-lens photolithography *Mater. Lett.* **209** 178–81
- [180] Emplit A, Lian J X, Huynen I, Vlad A and Sarrazin M 2014 Colloidal pattern replication through contact photolithography operated in a 'Talbot-Fabry-Perot' regime *Nanotechnology* **25** 145303
- [181] Lee I-H, Park S C and Lee S-D 2015 Submicro-pillars and holes from the depth-wise Talbot images of a conical phase mask *Opt. Express* **23** 25866–73
- [182] Chang Y-C, Wang S-M, Chung H-C, Tseng C-B and Chang S-H 2012 Observation of absorption-dominated bonding dark plasmon mode from metal-insulator-metal nanodisk arrays fabricated by nanospherical-lens lithography *ACS Nano* **6** 3390–6
- [183] Kim J, Cho K, Kim I, Kim W M, Lee T S and Lee K-S 2012 Fabrication of plasmonic nanodiscs by photonic nanojet lithography *Appl. Phys. Express* **5** 025201
- [184] Chang Y-C, Chung H-C, Lu S-C and Guo T-F 2013 A large-scale sub-100 nm Au nanodisk array fabricated using nanospherical-lens lithography: a low-cost localized surface plasmon resonance sensor *Nanotechnology* **24** 095302
- [185] Bonakdar A, Jang S J and Mohseni H 2014 Novel high-throughput and maskless photolithography to fabricate plasmonic molecules *J. Vac. Sci. Technol. B* **32** 020604
- [186] Qu C and Kinzel E C 2016 Polycrystalline metasurface perfect absorbers fabricated using microsphere photolithography *Opt. Lett.* **41** 3399–402
- [187] Qu C and Kinzel E C 2017 Infrared metasurfaces created with off-normal incidence microsphere photolithography *Opt. Express* **25** 12632–9
- [188] Wang L, Liu Z, Li Z, Zhang Y, Li H, Yi X, Wang J, Wang G and Li J 2017 Nanostructure nitride light emitting diodes via the Talbot effect using improved colloidal photolithography *Nanoscale* **9** 7021–6
- [189] Zhang Y, Wei T, Xiong Z, Shang L, Tian Y, Zhao Y, Zhou P, Wang J and Li J 2014 Enhanced optical power of GaN-based light-emitting diode with compound photonic crystals by multiple-exposure nanosphere-lens lithography *Appl. Phys. Lett.* **105** 013108
- [190] Hou C-H, Tseng S-Z, Chan C-H, Chen T-J, Chien H-T, Hsiao F-L, Chiu H-K, Lee C-C, Tsai Y-L and Chen C-C 2009 Output power enhancement of light-emitting diodes via two-dimensional hole arrays generated by a monolayer of microspheres *Appl. Phys. Lett.* **95** 133105
- [191] Zhang X A, Bagal A, Dandley E C, Zhao J, Oldham C J, Wu B-I, Parsons G N and Chang C-H 2015 Ordered 3D

- thin-shell nanolattice materials with near-unity refractive indices *Adv. Funct. Mater.* **25** 6644–9
- [192] Bagal A *et al* 2017 Large-area nanolattice film with enhanced modulus, hardness, and energy dissipation *Sci. Rep.* **7** 9145
- [193] Zhang X A, Chen Y-A, Bagal A and Chang C-H 2017 Enhanced total internal reflection using low-index nanolattice materials *Opt. Lett.* **42** 4123–6
- [194] Chattopadhyay S, Huang Y F, Jen Y J, Ganguly A, Chen K H and Chen L C 2010 Anti-reflecting and photonic nanostructures *Mater. Sci. Eng. R* **69** 1–35
- [195] Ho S-T, McCall S L, Slusher R E, Pfeiffer L N, West K W, Levi A F J, Blonder G E and Jewell J L 1990 High index contrast mirrors for optical microcavities *Appl. Phys. Lett.* **57** 1387
- [196] Schmidt M, Boettger G, Eich M, Morgenroth W, Huebner U, Boucher R, Meyer H G, Konjhodzic D, Bretinger H and Marlow F 2004 Ultralow refractive index substrates—a base for photonic crystal slab waveguides *Appl. Phys. Lett.* **85** 16–8
- [197] Marinelli C *et al* 2001 Design and performance analysis of deep-etch air/nitride distributed Bragg reflector gratings for AlInGaN laser diodes *Appl. Phys. Lett.* **79** 4076–8
- [198] Cho D, Park J, Kim J, Kim T, Kim J, Park I and Jeon S 2017 Three-dimensional continuous conductive nanostructure for highly sensitive and stretchable strain sensor *ACS Appl. Mater. Interfaces* **9** 17369–78
- [199] Bagal A, Dandley E, Zhao J, Zhang X A, Oldham C, Parsons G and Chang C-H 2015 Multifunctional nano-accordion structures for stretchable transparent conductors *Mater. Horiz.* **2** 486–94
- [200] Park S-G, Jeon T Y, Jeon H C, Yang S-M, Kwon J-D, Mun C-W, Cho B, Kim C S and Kim D-H 2014 Fabrication of 3D ZnO hollow shell structures by prism holographic lithography and atomic layer deposition *J. Mater. Chem. C* **2** 1957–61
- [201] Arpin K A *et al* 2013 Three-dimensional self-assembled photonic crystals with high temperature stability for thermal emission modification *Nat. Commun.* **4** 2630
- [202] Kim K, Park J, Hong S, Park S H, Jeon S G, Ahn C, Song J Y and Jeon S 2018 Anomalous thermoelectricity of pure ZnO from 3D continuous ultrathin nanoshell structures *Nanoscale* **10** 3046–52